Neurobiology of Disease 226 (2026) 107467

Contents lists available at ScienceDirect

Neurobiology of Disease

journal homepage: www.elsevier.com/locate/ynbdi

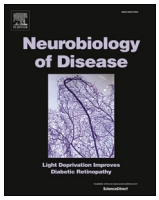

Early-onset neuroinflammation drives neurodegeneration caused by lysosomal PI(3,5)P_2 insufficiency

Bridget Wong [a], Morgan Payne [b], Alexander Silva [c], Emma Kurniawan [a], Alison S. Eidman [d,e], Donald Pizzo [a], Rachana Rajupalem [a], Guy M. Lenk [f], Joao A. Paulo [g], Taimur Khan [a], Eeva-Liisa Eskelinen [h], Steve P. Gygi [g], Nicholas G. Brown [d,e], Miriam H. Meisler [f], Andrew S. Mendiola [c], Brandon M. Gassaway [b], Cole J. Ferguson [a,*]

[a] Department of Pathology, University of California San Diego, San Diego, CA 92093, USA
[b] Department of Chemistry & Biochemistry, Brigham Young University, Provo, UT, USA
[c] Department of Pharmacology, University of California San Diego, San Diego, CA 92093, USA
[d] Department of Pharmacology, University of North Carolina School of Medicine, Chapel Hill, NC 27599, USA
[e] Lineberger Comprehensive Cancer Center, University of North Carolina School of Medicine, Chapel Hill, NC 27599, USA
[f] Department of Human Genetics, University of Michigan, Ann Arbor, MI 48103, USA
[g] Department of Cell Biology, Harvard Medical School, Boston, MA 02115, USA
[h] Institute of Biomedicine, University of Turku, Finland

ARTICLE INFO

Keywords:
Fig4
Vac14
PIKfyve
PI(3,5)P2
Phosphoinositide
Lysosome
Neuroinflammation
Astrocyte
Microglia
Reactive oxygen species
cGAS-STING
p53
Fas

ABSTRACT

Phosphatidylinositol 3,5-bisphosphate [PI(3,5)P_2] is a lysosomal signaling lipid whose deficiency, caused by mutations in the PIKfyve complex subunits *FIG4* or *VAC14*, underlies a spectrum of fatal neurologic diseases including Charcot-Marie-Tooth type 4J (CMT4J) and amyotrophic lateral sclerosis (ALS). To map the molecular consequences of PI(3,5)P_2 insufficiency in the brain, we performed quantitative proteomic and transcriptomic analyses of three mouse lines bearing distinct loss-of-function mutations in *Fig4* or *Vac14*, examining the brain at the presymptomatic and end stages. Strikingly, profound neuroinflammation was already present at postnatal day 5 (before significant neurodegeneration), characterized by complement activation, interferon signaling, and parenchymal infiltration of peripheral myeloid cells and T-cells. Isolated mutant microglia exhibited a markedly pro-oxidative transcriptional state with elevated reactive oxygen species, a partly non-cell-autonomous phenotype, being present in microglia from mice with conditional *Fig4* inactivation in just neurons and astrocytes. Comparison of early (P5) and late (P25) proteomics data revealed that PI(3,5)P_2 insufficiency impairs developmental remodeling of the brain proteome: proteins typically upregulated during postnatal maturation failed to accumulate, implicating lysosomal function in neurodevelopment. We identify coordinated elevation of p53, Fas receptor, inflammatory caspases, Gasdermin D, RIPK1, and ZBP1, consistent with multifactorial inflammatory cell death with features of apoptosis, pyroptosis, and necroptosis. Many of the dysregulated proteins are encoded by genes mutated in lysosomal storage disorders, ALS, CMT, Alzheimer's and Parkinson diseases, extending the pathogenic relevance of PI(3,5)P_2 insufficiency. Together, these findings establish that early neuroinflammation is a defining — and likely initiating — feature of neurodegeneration caused by disruption of lysosomal PI(3,5)P_2.

1. Introduction

Although known predominantly for their role in degrading and recycling proteins and organelles, lysosomes participate in a wide range of activities that enable cells to adapt to nutrient availability and metabolic demands, ranging from plasma membrane repair to cell signaling and immune recognition (Jain and Zoncu, 2026; Scott et al., 2025). It is therefore not surprising that perturbation of lysosome function is involved in the pathogenesis of many forms of neurodegeneration (Udayar et al., 2022), and that genes encoding lysosomal proteins have been implicated in a variety of inherited neurological disease beyond lysosomal storage disorders (Root et al., 2021). Indeed,

* Corresponding author at: Department of Pathology, University of California San Diego, San Diego, CA 92093, USA.
E-mail address: cferguson@health.ucsd.edu (C.J. Ferguson).

https://doi.org/10.1016/j.nbd.2026.107467
Received 12 May 2026; Received in revised form 31 May 2026; Accepted 1 June 2026
Available online 3 June 2026

even sporadic forms of neurodegeneration such as Alzheimer's disease, Parkinson's disease, and amyotrophic lateral sclerosis (ALS) share the feature of lysosomal dysfunction (Wallings et al., 2019). In such adult-onset proteinopathies, the cell's protein clearance system may be impaired by loss-of-function mutations in lysosome-autophagy pathway (Root et al., 2021) or by the lysosome becoming overwhelmed by aggregate-prone proteins (Nixon and Rubinsztein, 2024); in either case, evidence suggests that the neuron eventually succumbs to the accumulation of toxic proteins. Yet the pathogenesis of these diseases also involves neuroinflammation, which often occurs in the setting of lysosome dysfunction within glia (Quick et al., 2023) and is a common contributor to neurodegeneration. It is highly likely that non-degradative lysosomal activities become deranged in these diseases, but the number and variety of molecular pathways that could be involved makes distinguishing causal relationships a daunting challenge.

Given that damage to the lysosome itself can provoke inflammation (Scott et al., 2025), we wanted to explore how lysosome dysfunction contributes to neuroinflammation and begin to map the molecular changes that follow. To do so, we took advantage of mice bearing spontaneous mutations in the PIKfyve complex, which is the sole source of the signaling lipid phosphatidylinositol 3,5-bisphosphate [PI(3,5)P_2] that resides on the surface of lysosomal membranes. The PIKfyve complex, which is conserved from yeast to mammals, consists of a scaffolding protein, VAC14, to which the 5-kinase PIKfyve and 5-phosphatase FIG4 bind (Lees et al., 2020). Mutation in any of these three subunits impairs the synthesis of PI(3,5)P_2 as well as the downstream product PI5P (Rivero-Ríos and Weisman, 2022), hampering the lysosome's ability to recruit effectors, activate lysosomal ion channels, and carry out its digestive functions (Chen et al., 2017; Dong et al., 2010; Hasegawa et al., 2017; Ho et al., 2012; Wang et al., 2012). The brains of mice with loss-of-function mutations in *Fig4*, *Pikfyve* or *Vac14* display early-onset spongiform neurodegeneration (Chow et al., 2007; Ferguson et al., 2009, 2012; Jin et al., 2008; Lenk et al., 2011; Zhang et al., 2007; Zolov et al., 2012) accompanied by severe reactive astrogliosis (Ferguson et al., 2012; Ferguson et al., 2009). At the sub-cellular level, there is marked accumulation of macroautophagy intermediates and lysosome-related organelles within astrocytes and, to a lesser extent, neurons (Ferguson et al., 2010; Ferguson et al., 2009; Lenk et al., 2011). In humans, mutations of *FIG4*or *VAC14* result in severe neurological disease: dominantly inherited forms of amyotrophic lateral sclerosis (ALS) (Chow et al., 2009; Liu et al., 2022), a severe recessively inherited form of Charcot-Marie-Tooth disease (type 4 J) (Chow et al., 2007; Lenk et al., 2011; Nicholson et al., 2011), and several rare disorders that are fatal in infancy or childhood (Baulac et al., 2014; Campeau et al., 2013; Cuinat et al., 2025; Karaoğlu and Köse, 2021; Lenk et al., 2016). Since no *PIKfyve* variants have been identified in patients with neurologic disease, it is possible that consequential mutations are incompatible with survival.

In this study, we sought to gain insight into how PI(3,5)P_2 insufficiency and lysosomal dysfunction impacts the interactions between different cell types in the brain of mutant mice, and to establish the temporal relationship between neuroinflammation and the onset of neurodegeneration. We performed proteomic and transcriptomic analyses of the brain of *Fig4*and *Vac14* mutant mice, examining the proteome during both the first postnatal week and at a later stage (P25) prior to when mice die of severe neurodegeneration. We identified signatures of early-onset neuroinflammation involving peripheral immune cells and the adaptive immune system, and go on to demonstrate that immune dysregulation plays a more prominent role in the pathogenesis of neurodegeneration than previously appreciated, contributing to the failure of the early proteome in these mice to undergo normal developmental maturation. In addition to changes predicted from broad dysregulation of lysosome function, these analyses identified significant dysregulation of many proteins associated with the pathogenesis of common forms of neurodegeneration such as Alzheimer's disease (e.g. Apoe, Progranulin) and Parkinson's disease (e.g., Lrp10). These findings impact our understanding of the pathogenesis and therapeutic window for not just the diseases resulting from perturbation of PI(3,5)P_2, but also common forms of neurodegeneration in which lysosome dysfunction is increasingly implicated.

2. Results

2.1. Loss of Fig4 or Vac14 function causes accumulation of lysosome-related organelles in neurons and astrocytes

Global mutants homozygous for mutant *Fig4*or *Vac14* alleles exhibit impaired synthesis of PI(3,5)P_2, resulting in juvenile lethality from severe neurodegeneration (Chow et al., 2007; Jin et al., 2008). *Fig4* global mutant mice (*Fig4* $^{plt/plt}$) result from a spontaneous retrotransposon insertion in intron 18 that disrupts splicing of the *pale tremor* (*plt*) allele (Chow et al., 2007), leading to depletion of the Fig4 mRNA (Chow et al., 2007) and likely destabilizing the truncated protein. Inadequate Fig4 cannot activate the phosphoinositide 5-kinase PIKfyve via dephosphorylation (Lees et al., 2020; Strunk et al., 2020). Structural modeling demonstrated that the neurodegeneration-associated *Vac14* ^{L156R} mutation introduces a charged, bulky residue within a hydrophobic patch that interferes with binding of both PIKfyve and Fig4 to Vac14, impairing the 5-kinase activity of PIKfyve (Extended Data Fig. 1). Thus, both the *Fig4* ^{plt} and *Vac14* ^{L156R} mutations impair PI(3,5)P_2 synthesis and turnover. Although they may do so via distinct molecular mechanisms, the close similarity of the phenotypes of *Fig4* $^{plt/plt}$ and *Vac14* $^{L156R/L156R}$ mice indicates that PI(3,5)P_2 depletion drives pathogenesis in each case. We also generated a previously unpublished conditional *Fig4* $^{f/f}$,Nes-cre mutant that completely eliminates Fig4 in neurons and astrocytes but not in myelin-producing oligodendrocytes and microglia (resident innate immune cells in the brain) (Tronche et al., 1999). This mutant allows us to distinguish cell-autonomous effects of Fig4 loss in astrocytes and neurons from non-cell autonomous effects of Fig4 mutation in microglia and oligodendrocytes. The combination and timing of experimental approaches to studying these three models is laid out in Fig. 1a.

To ascertain the cellular manifestations of PI(3,5)P_2 deficiency in the brain, we performed transmission electron microscopy (TEM) in the cortex of mutant mice. Compared to the control cortex at postnatal day 21 (P21), in which cells contained just a few small lysosomes (Fig. 1b), the cortex of *Fig4* $^{plt/plt}$ mice contained many cells whose cytoplasm was almost totally occupied by lysosome-derived organelles, which are recognizable by their electron-dense, osmophilic lumens containing partially degraded cellular material (Fig. 1c). (Electron-lucent organelles with multilayered membranes containing encapsulated cytoplasm represent autophagosomes that have not yet fused with lysosomes to acquire their signature electron density.) Cells with marked accumulation of electron-dense lysosome-derived organelles were also present in the cortex of P21 *Vac14* mutant mice (Fig. 1d). Eccentrically located nuclei identify these cells as reactive astrocytes, an observation that agrees with previous fluorescence microscopy studies demonstrating that astrocytes accumulate the most lysosome-related organelles in the brain of both *Fig4* and *Vac14* mutants (Ferguson et al., 2012, 2009; Lenk et al., 2011).

Fig4 $^{f/f}$,Nes-cre mutant mice were severely affected from an early age and died around P12 (Fig. 1e), indicating that dysregulation of PI(3,5)P_2 just in neurons and astrocytes is sufficient for lethality. By age P10, the cortex of these mice exhibited spongiform neurodegeneration, a histopathologic pattern found in *Fig4* $^{plt/plt}$, *Vac14* $^{L156R/L156}$ and *Vac14* $^{-/-}$ mutant mice (Chow et al., 2007; Jin et al., 2008; Zhang et al., 2007) (Fig. 1f). TEM showed that the cytoplasm of reactive astrocytes was filled with lysosome-related organelles (Fig. 1g); neurons, identified by their abundant rough endoplasmic reticulum, also showed marked accumulation of electron-dense lysosome-related organelles (Fig. 1h). This finding is compatible with previous observations showing that autophagy intermediates accumulate in neurons of *Fig4* $^{plt/plt}$ global

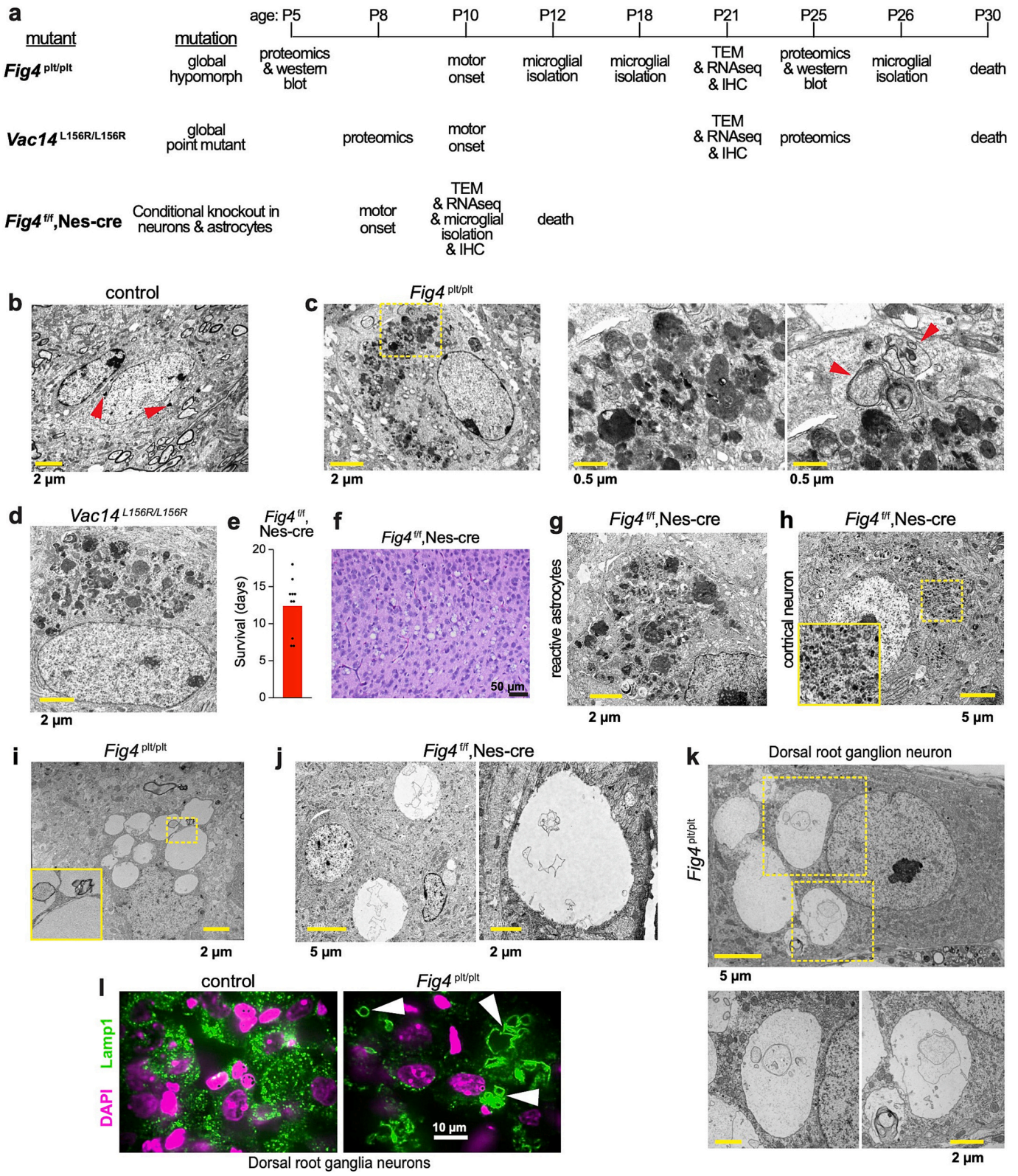

(caption on next page)

Fig. 1. Accumulation of lysosome-related organelles in the brain of mice with global or cell-specific dysregulation of PI(3,5)P_2.

a) Experimental timeline for studying the brain of each mutant mouse line.
b) Transmission electron microscopy (TEM) of the cortex of control mice at age P21. A few small lysosomes are labeled by arrowheads.
c) TEM of the cortex of *Fig4* global mutant mice. Reactive astrocytes contain many electron-dense lysosome-derived cytoplasmic organelles. Autophagosomes are labeled by arrowheads.
d) *Vac14* mutant cortex, showing accumulation of lysosome-related organelles within astrocytes.
e) Lifespan of *Fig4* $^{f/f}$ Nes-cre mice.
f) Hematoxylin and eosin staining of *Fig4* $^{f/f}$,Nes-cre cortex at age P10 showing cellular vacuolation and spongiform change.
g) Cortical astrocytes containing pathologic accumulation of lysosomes in *Fig4* $^{f/f}$,Nes-cre cortex at age P10.
h) Cortical neurons with pathologic accumulation of lysosomes in *Fig4* $^{f/f}$,Nes-cre cortex.
i) Empty-appearing vacuoles in cells from *Fig4* $^{plt/plt}$ cortex.
j) Vacuolated cells in *Fig4* $^{f/f}$,Nes-cre cortex.
k) Vacuoles in a neuron from *Fig4* $^{plt/plt}$ dorsal root ganglion (DRG).
l) Confocal immunofluorescence detection of lysosome-associated membrane protein 1 (LAMP1) in DRG neurons. Enlarged lysosomes indicated by the arrowheads.

mutants, albeit to a lesser degree than astrocytes (Ferguson et al., 2009).

In the brain of both *Fig4* $^{plt/plt}$ and *Fig4* $^{f/f}$,Nes-cre mice, we also observed cells with expanded cytoplasmic vacuoles that appeared largely empty, containing only a few membrane remnants (Fig. 1i,j). These vesicles are another cellular hallmark of impaired PI(3,5)P_2 synthesis (Chow et al., 2007; Jin et al., 2008; Zhang et al., 2007; Zolov et al., 2012) that likely results from inadequate activation of monovalent PI(3,5)P_2-dependent ion channels required for shrinking endolysosomal vesicles (Freeman et al., 2020). In global *Fig4* mutants, these enlarged vacuoles in neurons from dorsal root ganglia (where there are no astrocytes) were positive for Lamp1 (lysosome-associated membrane protein 1), supporting their endolysosomal identity (Fig. 1k,l).

These findings demonstrate that neurons and astrocytes exhibit multiple forms of lysosomal pathology when PI(3,5)P_2 synthesis is impaired.

2.2. Loss of Fig4 function impairs neurodevelopmental remodeling of the proteome

To capture changes in the brains of mutant mice at the protein level and determine how they evolve over time, we employed mass spectrometry (MS)-based proteomics with tandem mass tags (TMT) to simultaneously analyze the proteome of 16 samples (Fig. 2a): the 4 × 4 design allowed us to examine *Fig4* $^{plt/plt}$ during both the early (P5) and late stages (P25) of neurodegeneration. We included the entire brain as input to prioritize the identification of universally Fig4-dependent processes.

In volcano plots of the 10,509 quantified proteins (expressed as the ratio of their abundance in the mutant divided by control) versus significance, we see a rightward skew, indicating that protein excess prevailed at P5 (Fig. 2b and Supplementary Table 1). By P25, this surplus was more dramatic (Fig. 2c)—yet, strikingly, by this late timepoint there were nearly as many proteins in deficit as there were in excess. A tic-tac-toe plot of genotype differences in protein abundance at both timepoints confirmed that many proteins were in surplus at both timepoints, whereas undersupplied proteins appeared almost exclusively at P25 (Extended Data Fig. 2a). In PCA of proteomic data clustering samples by age and then genotype (control vs. *Fig4* $^{plt/plt}$; Fig. 2d), principal component 1 (PC1) reflected developmental stage and accounted for 81% of the variation between samples, demonstrating the remarkable degree to which the proteome is remodeled in the brain between the two timepoints. PC2, which accounted for 12% of the variation between samples, reflected genotype difference and showed enhanced separation at P25. Importantly, we observed reductions of Fig4 by 65% at the early timepoint and 60% at the late timepoint, validating the mass spectrometry-based quantitation (Fig. 2e). PIKfyve was also in deficit, confirming that loss of Fig4 destabilizes the PI(3,5)P_2 biosynthetic complex (Lees et al., 2020; Zhang et al., 2025).

To understand how the trajectories of protein excess and shortage differed, we set a threshold of <0.05 for the adjusted *p*-value and then depicted significantly altered proteins in heatmaps. The 2426 proteins that were overabundant at P25 tended to show a slight excess already by P5 (Fig. 2f). In contrast, the 2015 proteins that were in deficit had failed to undergo the typical process of developmental upregulation from P5 to P25 that occurred in the control brain (Fig. 2g). Mutation of *Fig4* therefore disrupts neurodevelopment in addition to inciting neurodegeneration.

2.3. Lysosome, immune, and metabolic functions become deranged by Fig. 4 or Vac14 mutation in the brain

To identify the molecular pathways dysregulated by *Fig4* mutation, we performed gene ontology (GO) analysis using ShinyGO (Ge et al., 2020). Similar GO terms came up for the significantly elevated proteins at both P5 and P25, so we opted to display GO analysis for just the early timepoint. As expected, cellular component GO terms reflected lysosomal dysfunction (Fig. 2h). But there was also strong enrichment for GO terms related to the immune response, indicating that neuroinflammation contributes early on potentially initiating the pathogenic cascade.

Proteins that were in short supply in the mutant brain at P25 were related to synaptic function, axons and dendrites, likely because neuronal loss has become so severe near the end stage in these animals (Fig. 2i, Extended Data Fig. 2b). Several components of myelin were also reduced, in agreement with previous reports that *Fig4* mutant mice largely fail to undergo myelination during development (Winters et al., 2011) (Extended Data Fig. 2c).

Metabolic pathways were among the few featuring both over- and under-abundant proteins, underscoring the complex relationship between lysosomal catabolism and the regulation of cellular energetics (Lawrence and Zoncu, 2019). Arginase 1 (Arg1), the single most highly elevated protein in the proteomics dataset from the Fig. 4 mutant brain (Extended Data Fig. 2d), is localized in lysosomes as well as mitochondria and is involved in metabolic activities such as ammonia detoxification. Arg1 was recently found to be expressed in a subset of microglia that have increased phagocytic activity and shape neural circuits during brain development (Stratoulias et al., 2023); Arg1-expressing microglia also reduce beta-amyloid plaque formation in the context of neuroinflammation (Cherry, 2015; Stratoulias et al., 2023) (Extended Data Fig. 2e). Recently, it was found that Arg1 overexpression in the context of ischemic vascular injury can stimulate the release of mitochondrial DNA into the cell, triggering inflammation via the cGAS-STING (cyclic GMP-AMP synthase-Stimulator of Interferon Genes) pathway (She et al., 2025).

We also carried out proteomic analysis of the brain of *Vac14* $^{L156R/L156R}$ mice. In this case, we employed an 18-plex TMT-MS design, inputting 4 replicates of whole brain at an early (P8) and 5 replicates at the late (P25) stage (Extended Data Fig. 3a and Supplementary Table 2). As was the case with *Fig4* global mutants, the proteomic perturbances in *Vac14* intensified with age (Extended Data Fig. 3b,c), as did the

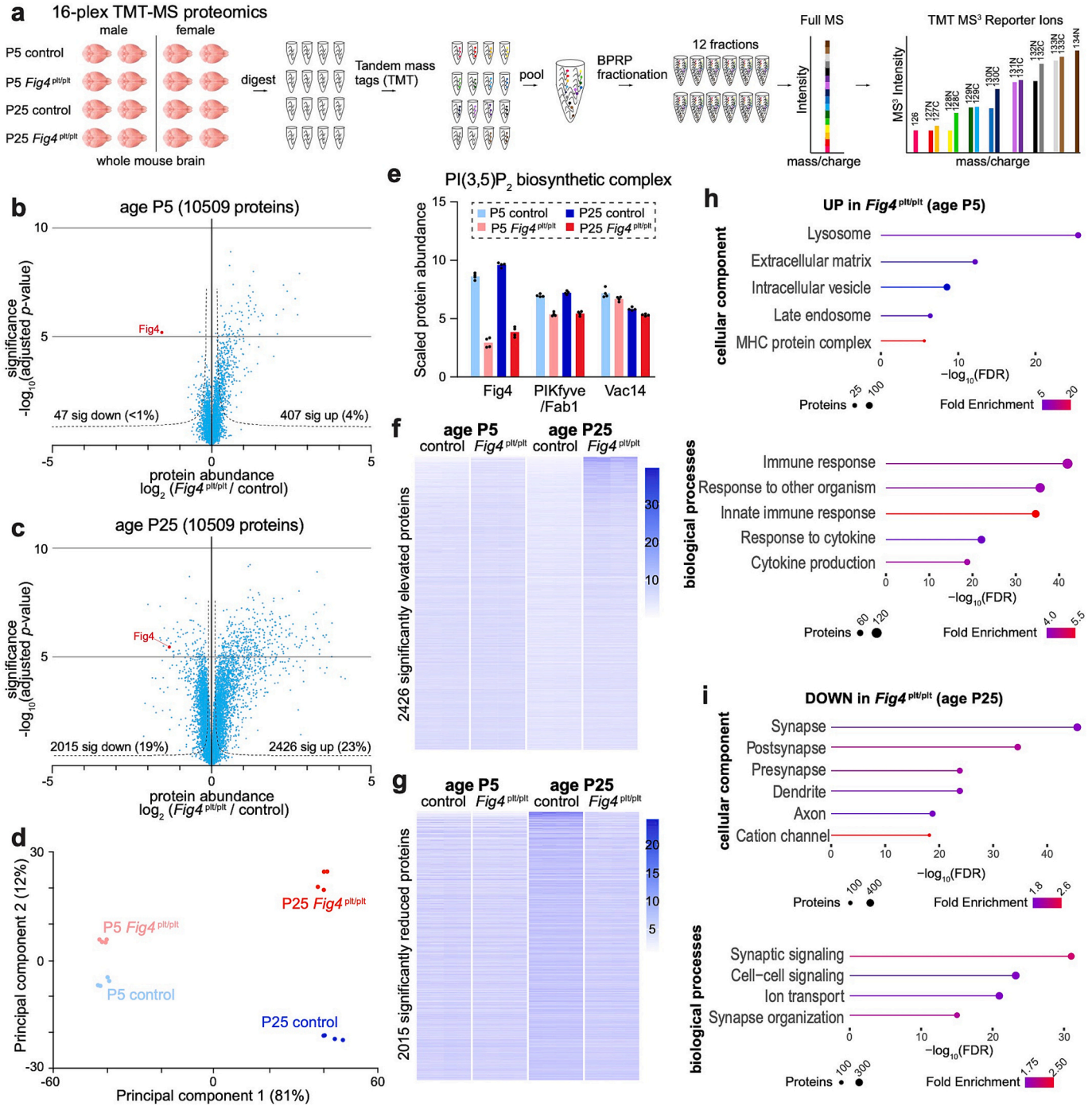

Fig. 2. Proteomic evaluation of the *Fig4* $^{plt/plt}$ brain reveals neurodegenerative and neurodevelopmental phenotypes.

a) Schematic of 16-plex tandem mass tag (() quantitative mass spectrometry (MS)-based proteomic evaluation of mouse brain at the indicated timepoints. $n = 4$ mice per group, including equal numbers of males and females.
b) Volcano plot depicting protein abundance versus significance at age P5. Significance thresholds (dotted lines) and adjusted *p*-values were determined using the Significance Analysis of Microarrays method (Tusher et al., 2001).
c) Volcano plot of data from the P25 timepoint.
d) PCA of proteomic data.
e) Abundance of components of the PIKfyve complex that regulates $PI(3,5)P_2$.
f) Heatmap of TMT-MS replicate data for all proteins that were significantly elevated (adjusted *p*-value <0.05) in the mutant brain at age P25. Replicate data for both genotypes at both timepoints are displayed.
g) Heatmap of TMT-MS data for all proteins that were significantly reduced in the mutant brain at age P25.
h) ShinyGO (Ge et al., 2020) gene ontology analysis of cellular components and biological process related to significantly elevated proteins in the *Fig4* mutant at age P5.
i) GO analysis of cellular components and biological process related to significantly reduced proteins at age P25.

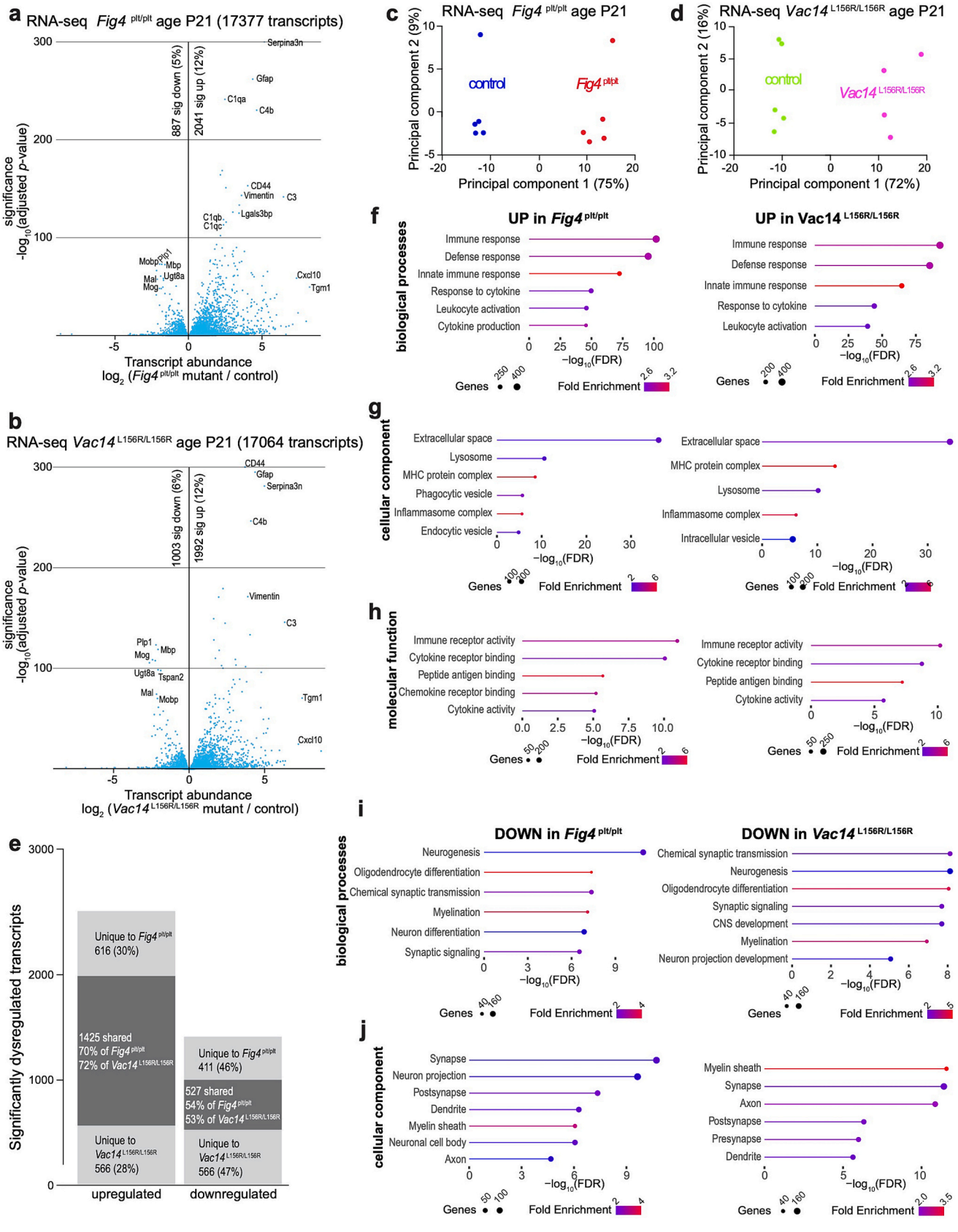

(caption on next page)

Fig. 3. Loss-of-function mutations in *Fig4* and *Vac14* perturb the brain transcriptome similarly.

a) Volcano plot from *Fig4* mutant cortex at age P21. Following extraction of total RNA from the cortex of P21 mice, depletion of ribosomal RNA, library preparation and cDNA sequencing, reads were aligned reads and DESeq2 (Love et al., 2014) was used for differential analysis and computation of adjusted *p*-values. The false discovery rate (FDR) threshold was <0.05.
b) RNAseq analysis of *Vac14* mutant cortex at age P21.
c) Principal component analysis (PCA) of biological replicates of RNAseq data from *Fig4* mutant cortex.
d) PCA of RNAseq data from *Vac14* mutant cortex.
e) Fraction of significantly dysregulated transcripts that overlap in RNAseq datasets for the two mutants.
f) f-h) GO analysis of biological processes for upregulated transcripts.
g) i-j) GO cellular component for downregulated transcripts.

separation between controls and mutants by PCA (Extended Data Fig. 3d). Homozygosity for the L156R point mutation led to a slight reduction in the abundance of Vac14 but did not affect PIKfyve (Fig4 was not detected in this dataset) (Extended Data Fig. 3e). Among significantly dysregulated proteins at P25, the patterns of protein elevation and depletion were the same as those observed in the *Fig4* mutant mice: proteins in the *Vac14* mutant brain that were modestly elevated at P8 became superabundant at P25, while proteins that were in deficit at P25 had failed to undergo developmental upregulation (Extended Data Fig. 3f-h). GO analysis yielded parallel results, with the most abundant proteins enriched in terms related to lysosome function and neuroinflammation, while there were deficits in proteins involved in neuronal components, neurodevelopment and myelination (Extended Data Fig. 4a-d).

2.4. Lysosome, immune, and neuronal functions are transcriptionally dysregulated in the brains of Fig4 and Vac14 mutants

As a complement to proteomic evaluation, we also performed RNAseq in the cortex of *Fig4* $^{plt/plt}$ and *Vac14* $^{L156R/L156R}$ mice at age P21. We detected 2041 elevated and 887 depleted mRNAs (out of 17,377 protein-coding transcripts) in the *Fig4* $^{plt/plt}$ cortex (Fig. 3a and Supplementary Table 3). In the *Vac14* mutant cortex, 1991 mRNAs were elevated and 1003 were depleted (out of 17,064 protein-coding transcripts) (Fig. 3b and Supplementary Table 4). Principal component analysis (PCA) segregated both mutants from their corresponding controls along the first principal component (Fig. 3c,d). The two mutant lines shared the vast majority of significantly elevated transcripts (Fig. 3e). This collection of upregulated transcripts is similar to those identified in prior studies of the astrocytic transcriptional response to neuroinflammation or ischemia (Zamanian et al., 2012), suggesting that astrocytes contribute to these elevated transcripts. A smaller fraction (but still the majority) of the significantly reduced transcripts also overlapped in the *Fig4* and *Vac14* mutants.

GO analysis of significantly elevated transcripts in both mutants identified biological processes related to immune response (Fig. 3f). Cellular components involved lysosomes and the major histocompatibility complex (MHC), while molecular functions reflected immune stimulation via the implication of cytokines and their receptors (Fig. 3g, h). In contrast, transcripts whose abundance was depleted in both mutants retrieved biological process GO terms related to neurogenesis and oligodendrocyte function (Fig. 3i), while cellular component GO terms relayed parts of neurons and myelin sheaths (Fig. 3j).

GO analysis of transcriptomic changes in the cortex of *Fig4* $^{f/f}$,Nes-cre mice at age P10—they do not survive long enough to be analyzed much later—revealed similar terms as in *Fig4* and *Vac14* global mutants (Extended Data Fig. 5a and Supplementary Table 5). The most significantly elevated transcripts among biological processes were again related to the immune response. Among cellular components, terms involved the extracellular space, MHCs, and lysosomes. Transcripts related to myelination were again significantly downregulated (Extended Data Fig. 5b-e). The main transcriptomic difference between the mutants is that the *Fig4* $^{f/f}$*,Nes-cre* mice lacked the downregulation of synapse-related GO pathways that showed up in the P21 *Fig4* and *Vac14* global mutants. This suggests either that neurodegeneration requires more time to unfold (P10 vs. P21 for the global mutants) or that intact Fig4 expression in oligodendrocytes and/or microglia stabilizes synapses in the face of neuronal Fig4 loss. Regardless, these observations show that deletion of Fig4 only in astrocytes and neurons is sufficient to initiate neuroinflammation and impede myelination.

2.5. Many of the dysregulated proteins in the mutant brain are associated with well-known neurodegenerative disorders and autoimmune diseases

A number of the proteins whose abundance was significantly altered in the brains of the mutant mice are associated with one or more of several classes of neurological disease: lysosomal storage disorders (LSDs); Charcot-Marie-Tooth neuropathies; Alzheimer's disease; Parkinson's disease and/or Lewy Body Dementia; ALS with or without frontotemporal dementia (FTD); and interferonopathies (see Table 1). Here we highlight a few of the most interesting findings, focusing on proteins in our mutant mice that were significantly dysregulated and whose genes are known to be mutated in human diseases.

Among the LSD-associated proteins was Progranulin, whose encoding gene *Grn* is mutated in neuronal ceroid lipofuscinosis (Kao et al., 2017) as well as in frontotemporal dementia (FTD) (Pottier et al., 2018; Yu et al., 2010) and Parkison disease (Reho et al., 2022).

Table 1
Proteins whose abundance is significantly altered in the bra**in of *Fig4* $^{plt/plt}$ and/or *Vac14* $^{L156R/L156R}$** mice at age P25 and whose encoding genes are mutated in the indicated neurodegenerative diseases. Bolded entries appear in more than one disease category. Underlined entries were significantly different (adjusted *p*-value <0.05) in proteomics data from both mutants; other proteins were significantly elevated or depleted just in the ***Fig4*** mutant.

Human Disease Category	Disease-associated proteins significantly altered in the P25 mutant brain
LSDs	*Increased*: Arsa, Arsb, Asah1, Ctsa, **Ctsc**, Ctsd, Ctsk, Fuca1, Gaa, Galc, Galns, **Gba1**, Gla, Glb1, Gm2a, Gns, **Grn**, Gusb, Hexa, Hexb, Hgsnat, Idua, Lamp2, Lipa, Man2b1, Manba, Mcoln1, Mfsd8, Naga, Naglu, Npc1, Npc2, Ppt1, Psap, Sgsh, Slc17a5, Sumf1, Tpp1 *Decreased:* Dnajc5, Fig4, Smpd1
Charcot-Marie Tooth	*Increased*: Aars1, Atp7a, Bag3, Hint1, Litaf, Lmna, Sbf2, Rab7a, Sord, **Sptlc1** *Decreased*: Atp1a1, Bscl2, Fig4, Gdap1, Inf2, Mfn2, Mtmr2, Nefl, Sbf1
Alzheimer	*Increased*: Abi3, Apoe, Casp7, Cd2ap, Clu, Cnn2, Gab2, **Grn,** Inpp5d, Lrp6, **Lrp10**, Ms4a4a, Plcg2, Psen2, Rin3, Sorl1, **Sqstm1**, Tmem106b, Trem2 *Decreased*: Bin1, Doc2a, Mef2c, Vps13c
Parkinson, Lewy Body Dementia	*Increased*: Atp13a2, Dzip1, **Gba1**, **Grn**, **Lrp10**, Rab32, Syt11 *Decreased*: Fbxo7, Nsf, Snca, Stk39, Unc13b, Vps13c
ALS, Frontotemporal Dementia	*Increased*: Ang, **Ctsc**, Hnrnpa2b1, Gle1, Glt8d1, **Grn**, **Lrp10**, Optn, Pon2, Pon3, Prph, Spg11, **Sptlc1**, **Sqstm1** *Decreased*: Atxn1, Atxn2, Chchd10, Dao, Erbb4, Fig4, Hnrnpa1, Mobp, Nefh, Nipa1, Sarm1, Sod1, Tuba4a, Vapb, Wdr7
Interferonopathy	*Increased*: Adar, Ddx58, Ifih1, Isg15, Pola1, Psmb8, Rnaseh2c, Samhd1, Trex1 *Decreased*: Lsm11

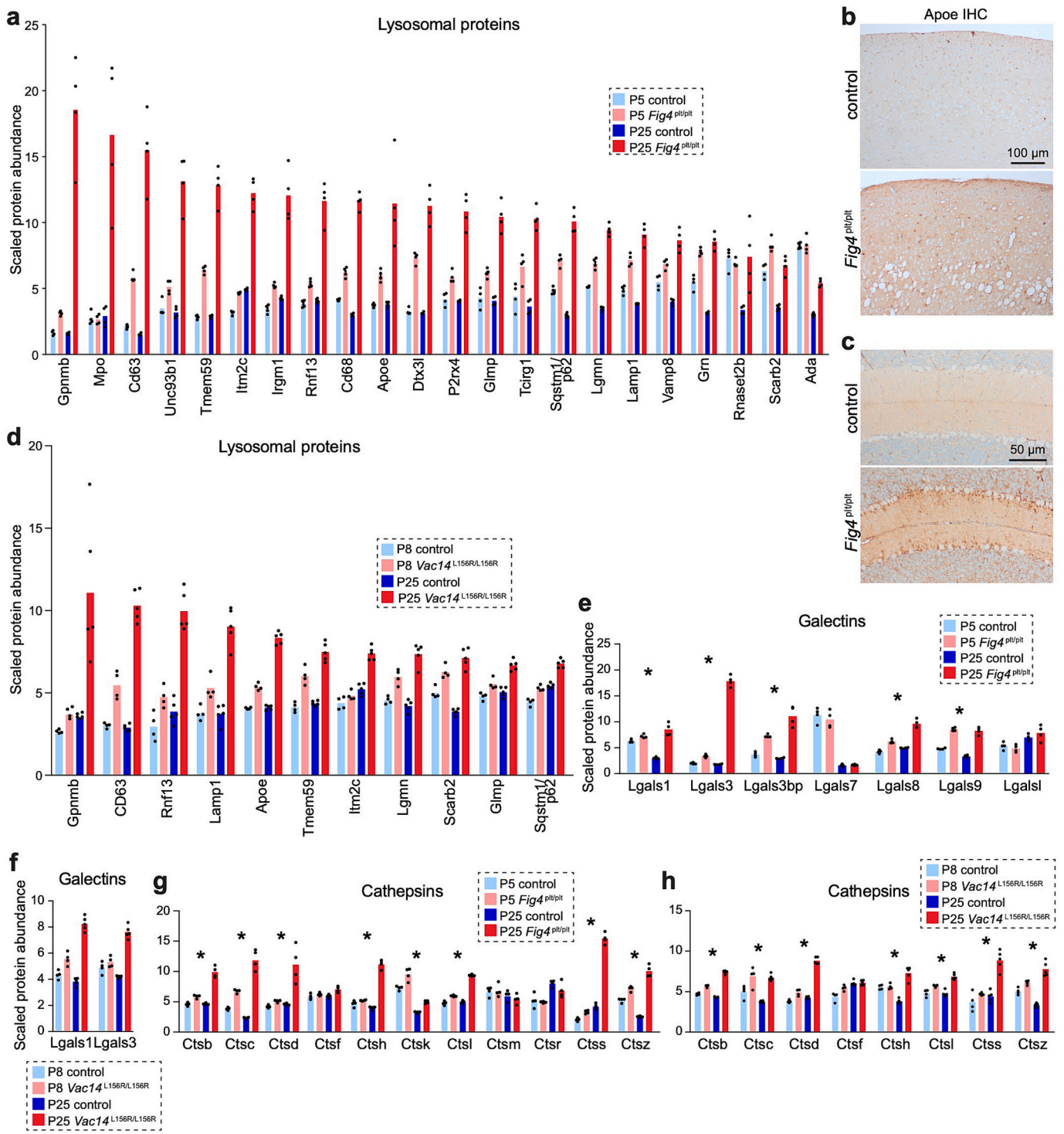

Fig. 4. Multiple disease-relevant lysosomal proteins are elevated in the *Fig4* and *Vac14* mutant brain.

a) Significantly elevated lysosomal proteins (adjusted *p*-value <0.05) detected using TMT-MS. Many of these are associated with the microglial lineage, others are membrane proteins, substrates or luminal enzymes.
b) Immunohistochemistry (IHC) of Apoe in formalin-fixed paraffin embedded cortex of *Fig4* mice at age P25.
c) Apoe IHC in the P25 cerebellum.
d) Bar graph depicting the scaled abundance of significantly elevated lysosomal proteins detected using TMT-MS in the *Vac14* mutant brain.
e) Abundance of galectins as detected by TMT-MS. Asterisks signify proteins which are significantly elevated at P25 (adjusted *p*-value <0.05).
f) Abundance of galectins 1 and 3 in the *Vac14* mutant, both of which are significantly increased at the late timepoint.
g) Abundance of cathepsin proteins in the *Fig4* mutant. Asterisks signify proteins which are significantly elevated at P25.
h) Abundance of cathepsins in the *Vac14* mutant.

Similarly, mutations in glucosylceramidase beta 1 (encoded by *Gba1* in mice and *GBA* in humans) cause the LSD Gaucher disease and represent a major risk factor for Parkinson's disease (Sidransky et al., 2009). Dozens of other lysosomal proteins were significantly elevated in proteomic analyses of the *Fig4* mutant brain, several of which are associated with the microglial lineage (including myeloperoxidase/Mpo, Cd63, Cd68), while others are membrane proteins (Lamp1, Glmp, Tcirg1, Vamp8, Scarb2/Limp2) or macroautophagy substrates (Sqstm1/p62) (Fig. 4a). Apoe, whose *APOE e4* allele in humans predisposes carriers to develop Alzheimer's disease (Chen et al., 2025), was elevated in proteomics and verified by immunohistochemistry (IHC) in the cortex and cerebellum of *Fig4* mutant mice (Fig. 4b,c). Several of the same lysosomal proteins were elevated in the brain of *Vac14* $^{L156R/L156R}$ mice (Fig. 4d, Table 1). To confirm that lysosome-derived organelles are overabundant, we tested activity toward nitrophenol-labeled β-galactose, β-glucuronide or β-hexose (substrates broken down by the lysosomal hydrolases β-galactosidase, β-glucuronidase and β-hexosaminidase, respectively) and found it increased in lysates from the mutant brain (Extended Data Fig. 6a). Multiple members of the Lipoprotein receptor-related protein family, which transport extracellular ligands to lysosomes for degradation, were also elevated in the *Fig4* mutant brain. Among these, Lrp4 and Lrp6 are known to regulate synapse function and maintenance (Buechler and Salinas, 2018; Chen et al., 2024) (Extended Data Fig. 6b). Mutations in Lrp10, the most significantly elevated member of this class, underlie genetic forms of ALS, Parkinson's disease, and dementia with Lewy bodies (LBD) (Quadri et al., 2018) (Table 1). Lrp10 also regulates trafficking of Amyloid Precursor protein, whose cleavage products produce the amyloid-beta peptides that accumulate in the hallmark plaques of Alzheimer's disease (Brodeur et al., 2012).

Five members of the galectin protein family, which are involved in cell-cell interactions, suppressing immune activation, and apoptosis, among other functions (Liu and Stowell, 2023), were significantly elevated in the *Fig4* mutant brain (Fig. 4e). Lgals1 and Lgals3 were also elevated in the *Vac14* mutant (Fig. 4f). Lgals3 senses lysosomal integrity and is recruited to damaged lysosomal membranes (Jia et al., 2020), indicating that perturbation of $PI(3,5)P_2$ activates galectin-mediated surveillance pathways. This observation accords with a recent study showing that the PIKfyve complex promotes lysosomal repair (Kutchukian et al., 2025). The highly elevated Gpnmb is also a biomarker of lysosome dysfunction (Van Der Lienden et al., 2018) (Fig. 4a,d). Eight out of eleven detected Cathepsins were elevated in the *Fig4* mutant brain (Fig. 4g), seven of which were also overabundant in the *Vac14* mutant (Fig. 4h). Cathepsins are lysosomal proteases that promote clearance of aggregated proteins and influence microglial-mediated neuroinflammation (Lewandowski et al., 2025). Transcripts encoding multiple Cathepsins were elevated in RNAseq data from the *Fig4* and the *Vac14* mutant cortices (Extended Data Fig. 6c). Induction of galectins, lysosome-associated membrane protein 2 (Lamp2) as well as several cathepsins was also observed RNAseq analysis of the brain of *Fig4* $^{f/f}$,Nes-cre mice, indicating that Fig4 loss in just neurons and astrocytes is sufficient to upregulate expression of essential lysosomal genes (Extended Data Fig. 6d,e).

2.6. Neuroinflammation takes place early in the context of $PI(3,5)P_2$ insufficiency

An unexpected finding from proteomic and transcriptomic profiling was the early appearance of a heightened immune response in the brain of *Fig4* and *Vac14* mutant mice (Fig. 5a,b). Even at the early timepoint, several components of the innate immune response were already highly elevated—Oasl1a and Oasl2 (members of the 2–5-Oligoadenylate synthetase-like family, proteins required for the antiviral activity of interferons (Chebath et al., 1987)) and Bst2/Tetherin (Fig. 5a), as were components of the Major Histocompatibility Complex (MHC) class 1 (H2-K1 and H2-D1) and MHC class 2 (H2-Eb1) (Fig. 5c). MHC proteins play multiple roles in neurophysiology (Cebrian et al., 2014; Elmer and McAllister, 2012; Nardo et al., 2016), but their abundance here may reflect the cell's attempt to compensate for impaired lysosome function: a specific version of the proteasome organelle known as the immunoproteasome facilitates proteolysis and antigen presentation via MHC class I, and the three proteasome subunits that were overly abundant—Psmb8 (Lmp7, β5i catalytic subunit, also elevated in *Vac14*), Psmb9 (Lmp2, β1i catalytic subunit) and Psmb10 (Mecl1, β2i catalytic subunit) (Fig. 5d, e) — are present specifically in the immunoproteasome (Murata et al., 2018). As is often the case, however, compensatory mechanisms can lead to further pathogenesis: neuronal expression of immunoproteasome-specific subunits promotes neurotoxicity during neuroinflammation by causing overexpression of the central metabolic regulator Pfkfb3 (Woo et al., 2025), which was elevated in the *Fig4* mutant brain at P25 (Extended Data Fig. 6d). The *Fig4* mutant brain also showed elevation of the Sting1 and Ddx58 components of the aforementioned cGAS-STING pathway, innate immune regulators that detect the presence of cytosolic DNA from mitochondria or nuclei undergoing lysis (Huang et al., 2023; Paul et al., 2021) (Fig. 5f). These proteomic signatures of immune activation are consistent with our transcriptomic data from the brains of both global *Fig4* and *Vac14* mutants showing upregulated expression of the complement cascade, which amplifies the response to pathogens and damaged cells. Of its constituent ~40 proteins, 16 components of the classical pathway were highly induced, including C1qa, C1qb, C1qc and C3, which mediate synapse loss in Alzheimer models (Hong et al., 2016) (Extended Data Fig. 7). Loss of Fig4 specifically in neurons and astrocytes of *Fig4* $^{f/f}$,Nes-cre mutant mice stimulated components of MHC classes 1 and 2, the immunoproteasome (Psmb8 and Psmb9), the classical complement cascade (Extended Data Fig. 8a-c), and interferon-response pathways (Extended Data Fig. 8d). These findings indicate that innate immune activation and interferon signaling contribute to the pathogenesis of neurodegeneration in the context of insufficient $PI(3,5)P_2$.

We also found massively induced expression of the chemokines Cxcl9, Cxcl10 and Cxcl11, which promote T-cell trafficking into the brain during neuroinflammation (Müller et al., 2010) (Fig. 5g). T-cells, and the adaptive immune system more broadly, have recently garnered attention as pathogenic drivers in Alzheimer's disease based upon the observation that they congregate in regions of tau accumulation and T-cell depletion ameliorates neurodegeneration in mouse models (Chen et al., 2023). To determine whether T-cells also infiltrate parenchyma of the $PI(3,5)P_2$ deficient mutant brain, we performed immunohistochemical staining with the T-cell marker CD3, which revealed many positive cells in multiple regions of the brain of *Fig4* mutant mice at age P21 (Fig. 5h). Aggregated CD3-positive cells surrounded zones of spongiform neurodegeneration in the *Vac14* mutant (Fig. 5i), and T-cells could be seen transmigrating through vessel walls (Fig. 5j). Thus, our results provide an additional neurodegenerative context in which the adaptive immune system contributes to neuroinflammation.

In such a profoundly inflammatory environment, it is perhaps not surprising that metallothioneins were among the most highly elevated proteins in the *Fig4* mutant brain (Fig. 5k). Apart from binding heavy metals to facilitate their clearance via lysosomes, metallothioneins have roles in antioxidant defense, neuroprotection, and glial reactivity, so their upregulation in the *Fig4* mutant model likely represents a compensatory response under conditions of chronic cellular stress (Bolognin et al., 2014; Nakamura et al., 2018; Pedersen et al., 2009).

2.7. Microglia and peripheral myeloid cells promote a neuroinflammatory oxidative state

The prominence of early neuroinflammation prompted us to directly examine the function of microglia, resident innate immune cells in the central nervous system. Transcriptomic data from the brain of global *Fig4* and *Vac14* mutant mice showed a striking elevation of mRNAs encoding the chemokines Ccl2, Ccl3, Ccl4 and Ccl5, which are expressed

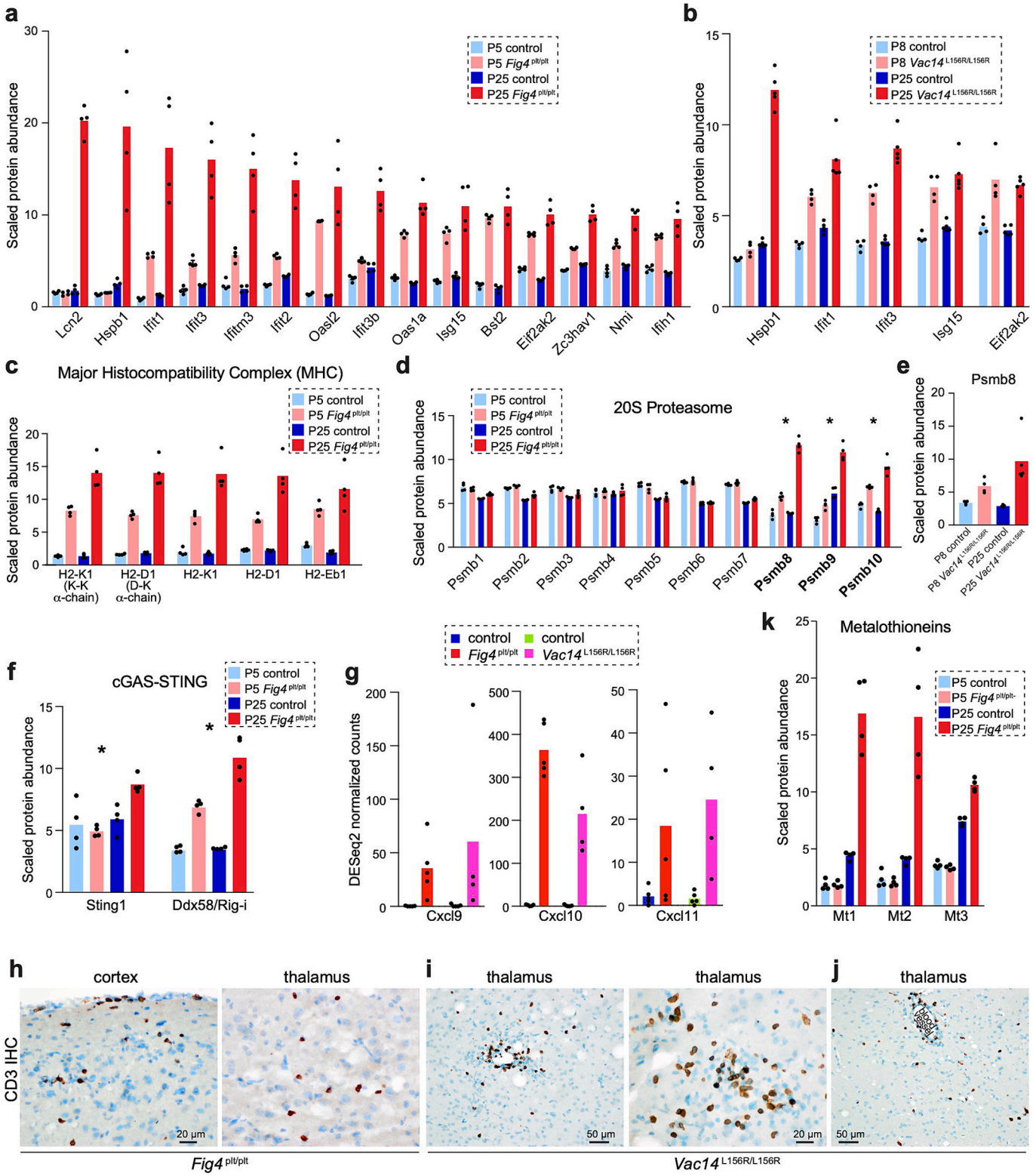

(caption on next page)

Fig. 5. Inflammatory proteins are highly elevated early on in the *Fig4* and *Vac14* mutant brains.

a) Bar graph showing significantly elevated immune-related proteins in the *Fig4* mutant at age P25, as measured by TMT-MS. Multiple members of the Ifit class (Interferon Induced proteins with Tetratricopeptide repeats), including Ifit1, Ifit2, Ifit3 and Ifitm3 were highly elevated in the *Fig4* mutant brain at the late timepoint
b) Significantly elevated immune-related proteins in the *Vac14* mutant brain at age P25.
c) Major histocompatibility complex (MHC) proteins that are significantly elevated in the *Fig4* mutant brain at age P25.
d) Abundance of components of the 20S proteasome. Asterisks mark significantly elevated proteins in the *Fig4* mutant brain at age P25. Immunoproteasome components appear in bold font.
e) Abundance of the immunoproteasome component Psmb8 in the *Vac14* mutant.
f) Abundance of cGAS-STING components, which control innate immune activation in the brain, which are significantly elevated in the *Fig4* mutant brain at age P25.
g) Significantly elevated metal-binding metallothionein proteins in the *Fig4* mutant brain.
h) Abundance of transcripts encoding inflammatory chemokines, as determined by RNAseq.
i) IHC detection of the pan-T-cell marker CD3 in the *Fig4* mutant. T-cells are exceptionally rare in the brain of unaffected mice.
j) CD3 IHC in the *Vac14* mutant.
k) T-cells entering by transmigrating through a blood vessel.

by microglia to recruit leukocytes during neuronal injury (Babcock et al., 2003) (Fig. 6a). Proteomics data showed elevation of multiple microglia markers, including Ptprc (CD45, leukocyte common antigen), Aif1 (Iba1), Itgam (CD11b) and Trem2, in the *Fig4* mutant brain (Fig. 6b). CD45 and Cd11b were also elevated in the *Vac14* mutant brain (Fig. 6c). Toll-like receptors 2, 3 and 7, which are abundant microglial cell-surface receptors (Kumar, 2019), were overabundant at the P25 timepoint in the mutant brain (Fig. 6d). Antibody staining of Iba1 showed severe microgliosis in the cortex of the *Fig4* global mutant (Fig. 6e). Iba1 staining was also increased in the hippocampal formation and cortex of mice with mutation of *Vac14*, while CD11b staining revealed microgliosis in the periaqueductal gray matter (Fig. 6f,g). Staining of Trem2, mutation of which is a risk factor for Alzheimer's disease and whose expression is linked to disease-associated microglia (Andersson-Rolf et al., 2017), in *Fig4* and *Vac14* mutant brains highlights the activation and proliferation of microglia (Fig. 6h).

Next we used fluorescence-activated cell sorting (FACS) to analyze immune cells in the brain. A gating strategy based upon the abundance of CD45 and CD11b separated microglia from peripheral myeloid cells, which infiltrate the parenchyma of the brain in conditions of severe inflammation (Kodosaki et al., 2024) (Fig. 6i, Extended Data 9a). Myeloid cells were rare in the control brain but much more populous in the *Fig4* mutant brain, such that by age P18 there was an inversion in the microglia/myeloid ratio, with microglia constituting just 24.1% of CD45-positive cells and myeloid cells nearly 50% (Fig. 6j,k).

Neuroinflammation is often accompanied by elevation of reactive oxygen species (ROS), which exacerbates neurotoxicity by damaging organelles and macromolecules. We measured ROS in microglia using DCFDA (2′,7′-dichlorodihydrofluorescein diacetate), a cell-permeable fluorogenic probe. Counting microglia that exceeded our fluorescence intensity threshold, we observed many more ROS^{HI} microglia in the *Fig4* mutant brain at age P18, when around half of microglia exceeded the threshold (Fig. 6l-n). The intensity of DCFDA fluorescence was also shifted higher on average at the population level in mutant microglia (Fig. 6o).

To determine if similar phenotypes in microglia could arise following conditional Fig4 loss in neurons and astrocytes, we also examined microglia and myeloid cells from the brain of *Fig4* $^{f/f}$,Nes-cre mice at age P10. Infiltrating myeloid cells were more abundant in the mutant brain, but the effect was modest (Extended Data Fig. 9b). Microglia (which do not utilize the Nestin promoter and therefore should maintain Fig4 expression) also exhibited an increase in DCFDA fluorescence and the fraction of cells with high ROS, suggesting this phenotype is at least partly non-cell autonomous (Extended Data Fig. 9c-e).

To gain insight into microglial dysfunction in the *Fig4* mutant brain, we isolated these cells to profile their transcriptome. PCA performed on RNAseq data at age P18 clustered samples according to genotype along principal component 1, which accounted for 73% of the variation between samples (Fig. 6p and Supplementary Table 6). Among the 13,268 detected transcripts, 1681 were significantly elevated and 1521 significantly depleted, indicating pervasive derangement of the transcriptional state of microglia (Fig. 6q). Interferon-response genes were much more highly expressed in mutant microglia. Interestingly, *Irf7* expression was highly elevated, whereas expression of *Irf3* was not (Fig. 6r,s). Both *Irf7* and *Irf3* encode transcription factors involved in the innate immune response, particularly the production of type I interferons and interferon-stimulated genes (Jefferies, 2019). Therefore, loss of Fig4 provokes a specific pattern of transcriptional changes driven at least in part by Irf7 but not Irf3. Microglial expression of the *Cxcl10* receptor was also upregulated, a phenomenon that occurs in response to brain injury or infection (Müller et al., 2010) (Fig. 6t).

Examination of the transcriptome of microglia isolated from the brain of *Fig4* $^{f/f}$,Nes-cre mice at by PCA separated the two genotypes along the first principal component (Extended Data Fig. 9f and Supplementary Table 7). Among the 11,815 transcripts detected, 343 were significantly upregulated with 137 downregulated—far fewer than in the *Fig4* global mutant (Extended Data Fig. 9g). These findings indicate that changes in the transcriptional state of microglia originate from both cell-intrinsic and cell-extrinsic effects of *Fig4* mutation.

Finally, we examined the transcriptome of *Fig4* mutant microglia within previously defined gene sets that are upregulated in response to severe neuroinflammation in the experimental autoimmune encephalomyelitis (EAE) model (Mendiola et al., 2020). These genes fall into three pathways—oxidative stress, lysosome & lipid, and type I interferon. Most of these transcripts were elevated in the transcriptome of microglia isolated from the brain of *Fig4* $^{plt/plt}$ at ages P12 and P26, with greater elevations at the later timepoint, particularly for genes related to interferon signaling (Extended Data Fig. 10a-c and Supplementary Tables 8 and 9). The fact that the same pathways were also induced in Fig4-expressing microglia isolated from the brain of *Fig4* $^{f/f}$,Nes-cre mice confirms that loss of Fig4 solely in neurons and astrocytes has non-cell-autonomous effects on microglia (Extended Data Fig. 10d-f).

2.8. Mutation of *Fig4* or *Vac14* causes inflammatory cell death in the brain

After transcriptomic and proteomic analyses revealed multiple connections between lysosome dysfunction and immune activation during neurodegeneration, we wondered whether these datasets could also shed light on whether inflammation played a role in cell death. Proteomic data identified several molecules related to the tumor suppressor p53 that were elevated at the late stage in the *Fig4* mutant brain (Fig. 7a). The p53 transcript itself (encoded by the *Trp53* gene in mice) was overexpressed in the cortex of both the *Fig4* and *Vac14* global mutants (Fig. 7b). Although p53 was not detected in our proteomics data, we could detect p53 in brain lysates by immunoblot, where p53 degradation products accumulated in the brain of *Fig4* mutants at P25 (Fig. 7c and Extended Data Fig. 11a). Fractionation of brain lysates into detergent-soluble (supernatant) and insoluble (pellet) fractions demonstrated that p53 degradation products accumulated over time,

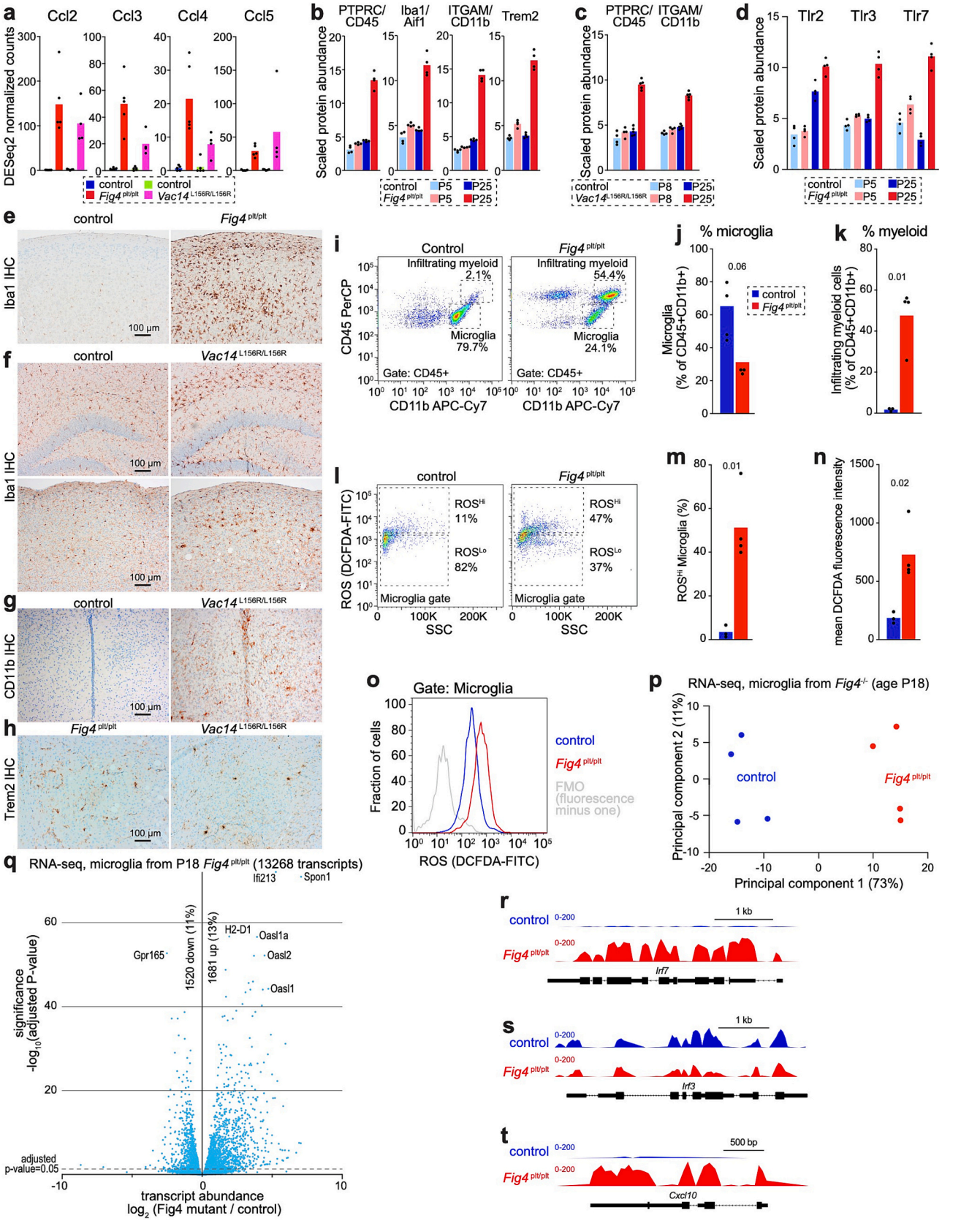

(caption on next page)

Fig. 6. Mutant microglia adopt a pro-oxidative inflammatory state.

a) Abundance of transcripts encoding inflammatory chemoattractant chemokines, as determined by RNAseq.
b) Significantly elevated microglial proteins in the *Fig4* mutant, as detected using TMT-MS.
c) Elevated microglial proteins in the *Vac14* mutant.
d) Toll-like receptor proteins in the *Fig4* mutant.
e) IHC detection of the microglial marker Iba1 in the cortex at age P25.
f) Iba1 IHC in the *Vac14* mutant hippocampal formation and cortex at P25.
g) CD11b IHC in the periaqueductal gray matter of *Vac14* mutant at P25.
h) Trem2 IHC highlighting activated microglia in the thalamus of *Fig4* and *Vac14* mutants at age P25.
i) Flow cytometry analysis of microglia and infiltrating myeloid cells in the *Fig4* mutant brain at age P18.
j) Fraction of microglia over time in the *Fig4* mutant brain. *p*-value by Welch's *t*-test.
k) Fraction of infiltrating myeloid cells over time in the *Fig4* mutant brain. *p*-value by Welch's t-test.
l) Stratification of microglia from the P18 brain into ROS^{Hi} and ROS^{Lo} populations based upon the intensity of the ROS reporter DCFDA.
m) Fraction of ROS^{Hi} microglia at the indicated ages. *p*-value by Welch's t-test.
n) Mean DCFDA fluorescence intensity within microglia isolated at the indicated ages. *p*-value by Welch's t-test.
o) Histograms depicting DCFDA fluorescence at the population level.
p) Principal component analysis of RNAseq data from isolated microglia.
q) Volcano plot of RNAseq data from microglia isolated at age P18.
r) Genome browser view of *Irf7* RNA-seq data from microglia isolated at P18.
s) *Irf3* gene.
t) *Cxcl10* gene.

becoming much more abundant in the *Fig4* mutant brain at the late stage of neurodegeneration (Fig. 7d and Extended Data Fig. 11b-e). p53 immunoreactivity was enriched in the insoluble fraction that was also enriched for the astrocyte marker GFAP and the autophagy substrate Sqstm1/p62. p53 IHC in the hippocampal formation of *Fig4* mutants highlighted nuclei of cells whose location and cytomorphology indicated reactive astrocyte identity (Fig. 7e). p53-positive cells were also observed in the cortex of *Vac14* mutant mice at age p25 and *Fig4* $^{f/f}$,Nes-cre mice at age P10 (Fig. 7f,g). The number of p53-positive nuclei was elevated in the cortex of *Fig4* $^{plt/plt}$ global and *Fig4* $^{f/f}$,Nes-cre conditional mutants at ages P25 and P10, respectively (Fig. 7h,i). p53 positivity was exceedingly rare in the control brain, as these timepoints are well past the window when p53 participates in normal neurodevelopmental apoptosis (Miller et al., 2000).

The presence of Fas Receptor (Fas) on the surface of a cell can initiate cell-extrinsic apoptosis when it binds to its ligand FasL, which is typically expressed by activated astrocytes and microglia (Choi and Benveniste, 2004). The abundance of the Fas protein was elevated in the *Fig4* global mutant (Fig. 7a), and RNAseq demonstrated greater abundance of Fas transcript in both the *Fig4* and *Vac14* global mutants than in controls (Fig. 7j). IHC detection of Fas in the hippocampus of the *Fig4* global mutant highlighted many positive cells (Fig. 7k). We also observed striking increases in Fas staining in the corpus callosum, cortex and hippocampal formation of *Fig4* $^{f/f}$,Nes-cre mice, with many cells exhibiting cytomorphologic features characteristic of astrocytes (Fig. 7l). These findings implicate p53 and Fas in cell death due to lysosome dysfunction in the setting of *Fig4* mutation.

Proteomics analysis of the *Fig4* $^{plt/plt}$ global mutant brain demonstrated elevation of Caspases 1 and 8 (Casp1 and Casp8), which are associated with inflammatory cell death (Ai et al., 2024) (Fig. 7m). Fas recruits FADD (Fas-associated via death domain) to activate Casp8, which initiates the extrinsic apoptosis cascade. Casp8 promotes the assembly and stabilization of inflammasome complexes, which contribute to Casp1 activation. Inflammatory caspases 4 and 12 were also elevated in transcriptomic analyses of the *Fig4* and the *Vac14* mutant brain (Fig. 7n). Activation of Casp1 and Casp8 causes cleavage of Gasdermin D (Gsdmd), which was also elevated in proteomic and transcriptomic analyses (Fig. 7o,p). Cleaved Gsdmd promotes pore formation, membrane permeabilization and lytic cell death, typically in response to inflammation (Broz et al., 2020). Ripk1 (Receptor-Interacting serine/threonine-protein Kinase 1) and, to a lesser degree, Ripk2 and Ripk4 were all elevated in the *Fig4* mutant brain (Fig. 7q). Ripk1 is a central molecular hub that regulates the decision to undergo cell death via apoptosis or necroptosis (Mitroshina et al., 2023), in addition to inciting microglial activation in models of Alzheimer's disease (Ofengeim et al., 2017). Finally Zbp1, the innate immune sensor and upstream trigger of RIPK-dependent necroptosis was also highly elevated in the *Fig4* mutant brain (Fig. 7r). Coordinated elevation of these molecular mediators of cell death reveal that $PI(3,5)P_2$ insufficiency leads to a pattern of neuroinflammation and neurodegeneration that is similar to, but more severe and earlier acting, than observed in other types of neurodegenerative diseases.

3. Discussion

In this study, we identify multiple pathways that are dysregulated by perturbation of the PIKfyve complex in the brain. Although dysfunction of the PIKfyve complex reduces both $PI(3,5)P_2$ and PI5P (Rivero-Ríos and Weisman, 2022), we focus our discussion on $PI(3,5)P_2$ because its molecular functions, and therefore its pathogenic contributions, are better established (Hasegawa et al., 2017; Ho et al., 2012). However, the roles of PI5P in nuclear signaling, autophagy induction, and regulation of growth factor receptor trafficking (Hasegawa et al., 2017) indicate that PI5P reduction very likely contributes to several of the phenotypes we document.

A major mechanism by which $PI(3,5)P_2$ controls lysosome function is by directly modulating the activity of lysosomal ion channels and transporters. For instance, $PI(3,5)P_2$ binding to TRPML1 (transient receptor potential mucolipin-1 channel encoded by *Mcoln1*) gates calcium release from lysosomes to coordinate membrane fusion, autophagosome-lysosome docking, and lysosomal exocytosis (Chen et al., 2017; Dong et al., 2010; Gan et al., 2022). $PI(3,5)P_2$ also controls flux through the two-pore sodium channels TPC1 and TPC2, whose activity helps regulates vesicle shrinkage to control lysosome volume (Freeman et al., 2020; She et al., 2018; Wang et al., 2012), which is perturbed by $PI(3,5)P_2$ dysregulation. More recently, $PI(3,5)P_2$ was shown to inhibit the lysosomal Cl^-/H^+ antiporter ClC-7, thus $PI(3,5)P_2$ regulates lysosomal acidification (Cao et al., 2023; Leray et al., 2022). Remarkably, loss-of-function mutations in *Clcn7* (encoding ClC-7) cause a multisystem disorder featuring lysosomal neurodegeneration and albinism (Bose et al., 2023; Leray et al., 2022; Nicoli et al., 2019), recapitulating key aspects of Fig4 loss in mice. $PI(3,5)P_2$ also activates the lysosomal ion transporter ATP13A2, which is implicated in Parkinson's disease (Holemans et al., 2015). Therefore, the lysosomal channelopathy resulting from $PI(3,5)P_2$ insufficiency is likely to be multifactorial, simultaneously compromising flux of multiple essential cations and anions.

The most striking and unexpected discovery in this study was the

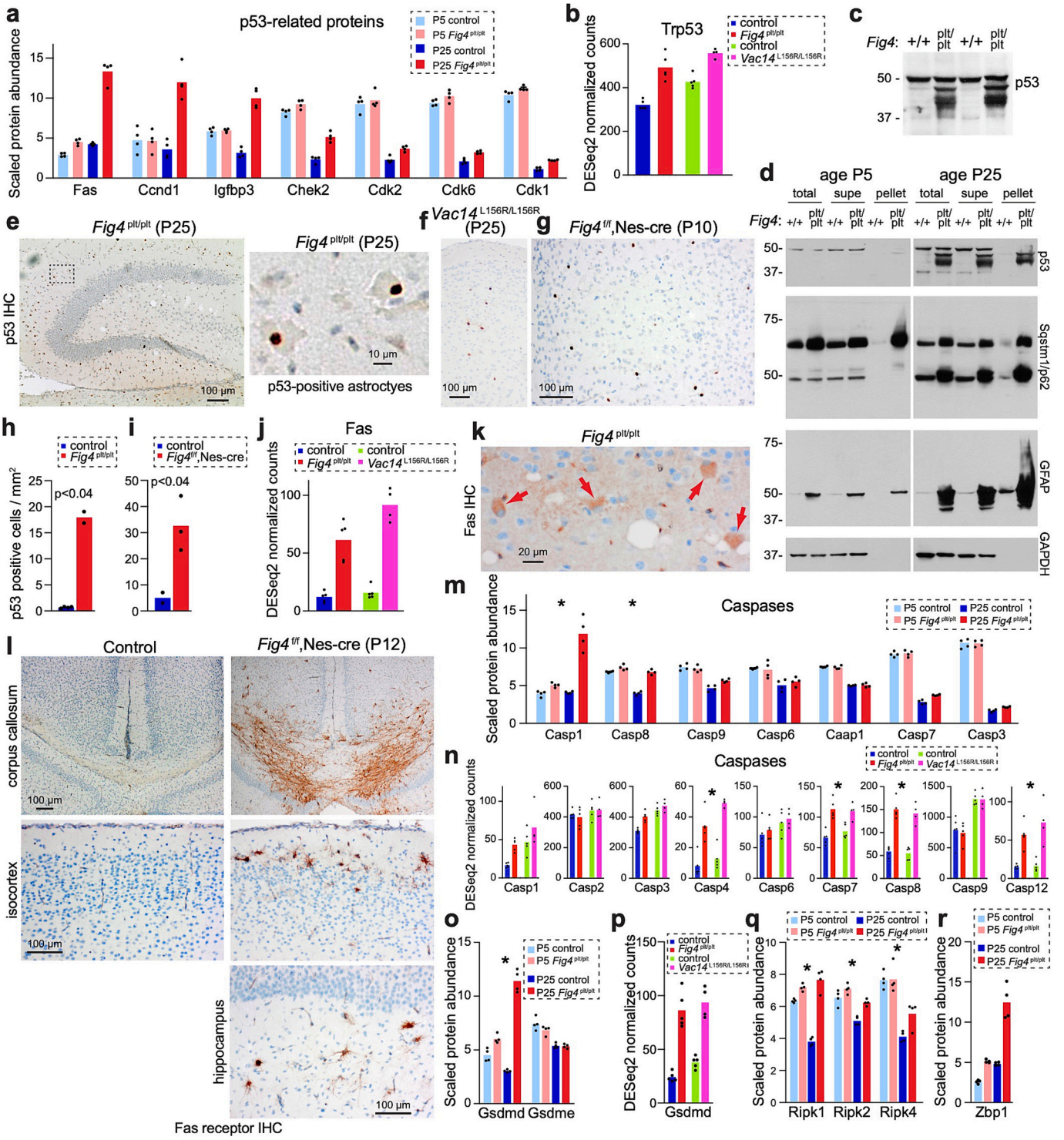

(caption on next page)

Fig. 7. Mutation of *Fig4* and *Vac14* causes multifactorial cell death of inflammatory etiology.

a) Abundance of significantly elevated p53-related proteins as detected by TMT-MS.
b) Normalized abundance of the *Trp53* transcript, as detected by RNAseq, in *Fig4* or *Vac14* mutant brain at age P21
c) Immunoblot detection of p53 in lysates prepared from replicates of the brain at age P25. Smaller bands likely represent partial degradation products.
d) Immunoblot detection of p53, p62, GFAP and GAPDH at P5 and P25. Total brain lysates were fractionated to generate detergent soluble and insoluble fractions. p53
e) IHC in the *Fig4* mutant hippocampus. p53 localizes to cells with cytomorphologic features of astrocytes.
f) p53 IHC in the *Vac14* mutant cortex.
g) p53 IHC in the cortex of *Fig4* $^{f/f}$,Nes-cre at P10.
h) Quantitation of p53 positive cells in the *Fig4* mutant cortex at age P25. *p*-value by unpaired two-tailed *t*-test.
i) Quantitation of p53 positive cells in the cortex of *Fig4* $^{f/f}$,Nes-cre. *p*-value by unpaired two-tailed t-test.
j) Normalized abundance of the Fas transcript in the *Fig4* and *Vac14* mutants, as measured using RNAseq.
k) Fas receptor IHC in the hippocampal formation of the *Fig4* mutant.
l) Fas IHC in multiple brain regions of the *Fig4* $^{f/f}$,Nes-cre.
m) Abundance of Caspase proteins in the *Fig4* mutant as detected by TMT-MS. Significantly elevated proteins are marked by asterisks. Caspases 1 & 8 are specifically associated with inflammatory cell death.
n) Normalized abundance of Caspase transcripts as measure by RNAseq in P21 cortex.
o) Abundance of Gasdermin proteins in the brain.
p) Normalized abundance of Gasdermin transcripts as measure by RNAseq in P21 cortex.
q) Abundance of Ripk proteins in the brain.
r) Abundance of Zbp1, an upstream activator of Ripk proteins in the brain.

severity of early neuroinflammation in these models. Neuroinflammation has complex, context-dependent and incompletely understood roles in neurodegeneration. During neuronal injury, regulated inflammation initially protects neurons from further damage. Chronic stimulation, however, as occurs in the most common forms of neurodegeneration (e.g., Alzheimer, Parkinson, and ALS), eventually deranges injury-responding glia (Shi and Yong, 2025), causing further neuroinflammation and perpetuating a vicious cycle that exacerbates and spreads injury (Dokalis and Prinz, 2019). In the case of diseases resulting from mutations in *FIG4* or *VAC14*, our data indicate that early neuroinflammation, coinciding with (or possibly contributing to) the failure of normal developmental maturation, initiates the conditions that lead to chronic inflammation and eventual cell death. The intensity of early neuroinflammation in *Fig4* and *Vac14* mutant mouse models connects lysosome dysfunction with pathologic immune activation in the brain. We previously demonstrated massive astrogliosis in these mutants (Ferguson et al., 2009); here we show that mutation of *Fig4* or *Vac14* also causes profound microgliosis, and microglia in the *Fig4* mutant brain adopt a markedly pro-inflammatory, pro-oxidative state. Lysosome dysfunction increases ROS generation (Nakanishi and Wu, 2009), which is increasingly recognized as pathologic driver in diverse forms of neurodegeneration (Angelova and Abramov, 2018). The observation that microglia from *Fig4* $^{f/f}$,Nes-cre mice also adopt a pro-inflammatory transcriptome accompanied by increased ROS indicates that this phenotype has a non-cell autonomous component resulting from Fig4 loss in neurons and/or astrocytes. In the global mutants, secretion of chemokines (likely originating from astrocytes and microglia) triggered parenchymal infiltration of not only peripheral myeloid cells but also T-cells, implicating the adaptive as well as innate immune system in pathogenesis and providing an additional setting in which T-cells contribute to neurodegeneration.

The observation that p53 accumulates in the brain of both *Fig4*- and *Vac14*-mutants provides the first evidence that mutations in the PIKfyve complex alter the abundance of any nuclear protein, although this effect could be indirect rather than a consequence of impaired lysosomal p53 degradation. Increased p53 occurs in conjunction with upregulation of several mediators of inflammatory cell death, including Fas receptor, inflammatory caspases 1 and 8, Ripk1, Zbp1 and Gasdermin D, which collectively reflect the consequences of unrestrained immune activation. Both Zbp1 and the highly upregulated cGAS-STING component Ddx58/RIG-I normally bind to cytoplasmic nucleic acids, as occurs during viral infection, but in the context of our mutants these factors are likely responding to cytoplasmic nucleic acids released by nuclei undergoing lysis.

The relationship between lysosomal dysfunction and cGAS-STING activation in the PI(3,5)P_2-deficient brain is likely to be multifaceted and self-amplifying. First, lysosomal membrane damage and leakage of lysosomal contents (probably including nucleic acids from partially degraded mitochondria) into the cytoplasm is expected to engage the cGAS sensor and initiate STING-dependent interferon signaling (Huang et al., 2023; Paul et al., 2021). Our observation that lysosomal integrity surveillance proteins such as galectin-3 are highly elevated in the mutant brain, couple with the PIKfyve complex's role in promoting lysosomal repair (Kutchukian et al., 2025), indicates that lysosomal membrane damage follows PI(3,5)P_2 insufficiency. Second, severe mitochondrial oxidative stress in mutant microglia would also promote mitochondrial DNA release into the cytoplasm, providing an additional cGAS-activating stimulus that is distinct from lysosomal damage per se (Huang et al., 2023). Third, and most directly relevant to the present study, PI(3,5)P_2 is an endogenous ligand of STING that promotes its oligomerization and activation (Tan et al., 2026). Perturbation of PI(3,5)P_2 could therefore dysregulate STING activation independently from nucleic acid sensing. Fourth, arginase 1 (Arg1), which ranks among the most highly elevated proteins proteome of the *Fig4* mutant brain, was recently shown to drive remodeling of mitochondrial cristae and release of mitochondrial DNA via a cGAS-STING-dependent mechanism following vascular dysfunction (She et al., 2025). Elevation of Arg1 in the PI(3,5)P_2-deficient brain could therefore amplify the interferon response. These convergent mechanisms suggest that cGAS-STING overactivation is an organizing central hub of the pathological inflammatory state in the PI(3,5)P_2-deficient brain. This mechanistic insight raises the possibility that cGAS-STING inhibitors, currently under investigation for common neurodegenerative diseases, may be particularly warranted to evaluate as therapeutic candidates in human diseases resulting from mutations in *FIG4* or *VAC14*.

Based upon the above combination of accumulated mediators of cell death, we infer that cell death occurs via a multifactorial inflammatory process with features of apoptosis, pyroptosis and necroptosis (Ai et al., 2024). Astrocytes, the primary cells in which lysosomes, p53 and Fas accumulate in the *Fig4* and *Vac14* mutant brain, are central regulators of necroptosis during inflammatory, ischemic or degenerative conditions in the brain (Mitroshina et al., 2023). The observation that iron-binding metallothionein proteins are elevated in the setting of a highly oxidative environment, combined with previous studies showing that PI(3,5)P_2 controls iron release from the endolysosomal channel TRPML1 (Chen et al., 2017; Dong et al., 2008), suggests that ferroptosis (Fei and Ding, 2024) could also occur in the brain of *Fig4* and *Vac14* mutants. Sorting out whether all these forms of cell death occur across the mutant

brain or whether specific cell death pathways favor particular brain regions or cell types will require additional experimentation in cell-specific conditional mutants.

In sum, we have identified multiple pathogenic mechanisms of neurodegeneration caused by impaired synthesis of lysosomal signaling lipids. Recent work on Alzheimer's disease, Parkinson's disease, and other neurodegenerative conditions has begun to tease out the influence of PI(3,5)P_2 insufficiency on the pathogenesis of these diseases, but, understandably, the focus has been on the canonical lysosomal degradative functions. Our observations greatly expand the scope of PI(3,5)P_2 effects by shedding light on the relationship between lysosomes, neuroinflammation and cell death. These findings carry relevance not only to -*FIG4*- and *VAC14*-related human neurodegenerative diseases, but also to all forms of neurodegeneration that arise from impaired lysosomal proteostasis.

4. Methods

4.1. Mice

Animals were cared for in accordance with NIH guidelines. All experimental methods were approved by the UCSD Institutional Committee on the Use and Care of Animals under the protocol number S20121. The previously described Fig. 4 (Chow et al., 2007) and Vac14 (Jin et al., 2008) global mutants were maintained as recombinant inbred strains by cousin mating. Mutants were generated by crossing heterozygotes. The *Fig4* $^{f/f}$,Nes-cre mice were generated by crossing *Fig4* $^{f/f}$ mice with *Fig4* $^{f/+}$,Nes-cre mice. *Fig4* $^{f/f}$ mice were kept separate and never exposed to Nes-cre to avoid germline recombination. When used in experiments, mice were deeply anesthetized with isofluorane and swiftly decapitated.

4.2. Structural analysis

The mouse Vac14-Fig4-PIKfyve complexes in both a 2:1:1 and 1:1:1 ratio were predicted using AlphaFold 3(Abramson et al., 2024). Models were analyzed and fit into cryo-EM density maps (EMD: 22631, EMD: 22647) using ChimeraX (Lees et al., 2020).

4.3. Transmission electron microscopy

Mice were deeply anesthetized and transcardially perfused with 2% paraformaldehyde (Electron Microscopy Sciences #15710) + 2.5% glutaraldehyde (Electron Microscopy Sciences #16120) in 0.15 M sodium cacodylate buffer (Electron Microscopy Sciences #12310) followed by postfixation in 1% OsO4 (Electron Microscopy Sciences #19151) in 0.15 M cacodylate buffer for 1 h on ice. The specimens were stained with 2% uranyl acetate (Ladd research #23620) for 1 h on ice, following graded dehydration in series of ethanol (50–100%) while remaining on ice. The specimens were then subjected to 1 wash with 100% ethanol and 2 washes with acetone (15 min each) and embedded with Durcupan (Sigma-Aldrich #44610-1EA). Sections were cut at 60 nm on a Leica UCT ultramicrotome, and picked up on 300 mesh copper grids (Electron Microscopy Sciences #T300H-Cu). Sections were post-stained with 2% uranyl acetate for 5 min and Sato's lead stain (1% lead acetate Electron Microscopy Sciences #17600, 1% Lead Nitrate (Electron Microscopy Sciences #17900), 1% Lead citrate (Electron Microscopy Sciences #17800) and 2% sodium citrate Electron Microscopy Sciences #21140) in water for 1 min. Finally, the sections were observed at the UCSD Electron Microscopy Core (UCSD-CMM-EM Core, RRID: SCR_022039), or at the Electron Microscopy Unit, Institute of Biotechnology, University of Helsinki, Finland, using a Jeol 1400 plus operated at 80KeV and equipped with a bottom-mounted Gatan One View camera.

4.4. Immunofluorescence in frozen sections

Freshly dissected mouse dorsal root ganglia were flash frozen in OCT before cutting 10 μm cryosections. Sections were dried at room temp for 20 min, fixed in fresh 3.2% paraformaldehyde (Pierce) for 20 min, permeabilized with 0.2% Saponin and blocked in 10% goat serum. Primary rat anti-LAMP-1 (DSHB Cat# 1d4b, RRID:AB_2134500) was used at a concentration of 1:500 was applied and sections were incubated overnight at 4 degrees in 2% goat serum. Secondary detection was carried out using Goat anti-rat antibodies conjugated to Alexa 488 (Thermo Fisher Scientific Cat# A-11006, RRID:AB_2534074) at dilutions of 1:1000. 1 μm confocal optical sections were acquired on a Zeiss LSM 510-META laser scanning confocal microscope, 3 of which were flattened via a maximum intensity *Z*-projection to generate the final images.

4.5. Mouse proteomic sample processing

Mouse brain was extracted and frozen in a dry ice ethanol slurry. Brains were then processed using the streamlined TMT labelling protocol as previously described (Ferguson et al., 2022; Ledvin et al., 2023; Navarrete-Perea et al., 2018). Processing included lysis with 8 M urea in 200 mM EPPS pH 8.5 with protease (Pierce A32953) and phosphatase (Pierce A32957) inhibitors, homogenization (Fisher Scientific Tissuemiser), sonication (Branson Digital Sonifier 450; 40% amplitude 30 s on, 30 s off for 4 cycles), reduction with 5 mM TCEP, alkylation with 10 mM iodoacetamide, and quenching with 5 mM DTT. This was followed by methanol/chloroform precipitation of 100 μg of protein, reconstitution in 200 mM EPPS pH 8.5, digestion overnight at 37 °C with 1:100 LysC and 1:100 trypsin. Peptides were labeled by adding anhydrous acetonitrile to ~30%, followed by labelling with TMTpro reagent (Thermo Scientific). 1% of each labeled sample was combined and analyzed unfractionated to ensure labeling efficiency was >97% and that the samples are mixed at a 1:1 (total amount) ratio across all conditions. After mixing, labeled peptide samples were de-salted using a 200 mg Sep-Pak cartridge (Waters WAT054925), followed by drying in a rotary evaporator. *Fig4* mutant samples were reconstituted in 5% ACN 10 mM ammonium bicarbonate and fractionated using basic pH reverse phase chromatography on an Agilent 1260 HPLC system using an Agilent 300extend-C18 column (3.5 μm, 4.6 × 250 mm). Peptides derived from the *Fig4* mutants and controls were then subjected to a 75 min linear gradient from 13% to 42% of Buffer B (10 mM ammonium bicarbonate, 90% ACN, pH 8) at a flow rate of 0.6 mL/min, resulting in a total of 96 fractions which were consolidated into 24 by combining (in a chessboard pattern) four alternating wells down columns of the 96-well plate. 12 samples were desalted via StageTip and resuspended in 5% ACN 1% formic acid for analysis on a Thermo Fisher Orbitrap Fusion Lumos. *Vac14* mutant samples were reconstituted in buffer A (10 mM ammonium formate in 3% ACN) and fractionated using basic pH reverse phase chromatography on a Gemini C18 column (3 μm, 2 × 50 mm, 110 Å). Peptides derived from the *Vac14* mutants and controls were subjected to a 41-min leaned gradient of 0% to 60% Buffer B (10 mM ammonium formate in 90% ACN) of 0.5 mL/min resulting in a total of 40 fractions that were concatenated from every other row in the same column into 20 samples. Samples from every other column (a total of 10) were desalted via StageTip and resuspended in 1% formic acid for analysis on a Thermo Fisher Orbitrap Astral (*Vac14* mutant and control).

4.6. Proteomic data collection

Mass spectra for the *Fig4* mutants and controls were collected on Orbitrap Fusion Lumos mass spectrometer (ThermoFisher Scientific) coupled to a nanoEASY-nLC 1200 LC pump (ThermoFisher Scientific). Peptides were separated on a 35 cm column (i.d. 100 μm, Accucore, 2.6 μm, 150 Å) packed in-house using a 90 min gradient (from 5% -30% acetonitrile with 0.1% formic acid) at 500 nL/min. Data was collected

using a hrMS2 method. MS1 data were collected using the Orbitrap (120,000 resolution; maximum injection time 50 ms; AGC 4e5, 400–1400 *m/z*). Determined charge states between 2 and 5 were required for sequencing and a 120 s dynamic exclusion window was used. MS2 scans consisted of higher collision energy dissociation (HCD) followed by Orbitrap analysis, with a resolution of 50,000, automatic gain control (AGC) 1.5E5, NCE (normalized collision energy) of 36, *q*-value 0.25, maximum injection time 250 ms, and isolation window of 0.5 Da using a Top10 method.

Mass spectra for the *Vac14* mutants and controls were collected on a Themo Fisher Orbitrap Astral Mass Spectrometer coupled to an Ultimate 3000 HPLC. Peptides were separated on a 15 cm 75 μm diameter column packed with Ultrapure Silica (2.0 μm, 100 Å) resin (Thermo Fisher Scientific) with a 60-min gradient of 5%–25% acetonitrile in 0.1% formic acid at a flow rate of 300 nL/min. Data was collected using a hrMS2 method. Precursors were collected with an orbitrap MS1 spectrum (60,000 resolution, Scan Range 400–1500, Automatic Gain Control (AGC) 200%, RF lens 50%, Maximum injection time 100 ms). The isolated precursors were fragmented with high-energy collision dissociation (HCD) at a normalized collision energy (NCE) of 35% and analyzed in the Astral (TMT on isolation window 0.5 m/z, AGC 100%, maximum injection time 25 ms, Scan Range 110–2000 m/z).

The TMT ProteomeXchange Consortium via the PRIDE (Perez-Riverol et al., 2019) partner repository with the dataset identifiers PXD066767 (*Fig4* mutant) and PXD066776 (*Vac14* mutant).

4.7. Mass spectrometry data processing

Mass spectra were processed using a COMET (Eng et al., 2013)-based (version 2020.01 rev. 4) software pipeline. Data for *Fig4* mutants and controls was searched against the UniProt (The Uniprot Consortium, 2023) Mouse (1/26/2022, 63,780 sequences) database while data for *Vac14* mutants and controls was searched against UniProt Mouse (10/03/2024, 54,855 sequences) database. Protein measurements for experiments with both *Fig4* and *Vac14* mutant, data were searched with a 20-ppm precursor ion tolerance and 0.02 Da product ion tolerance. TMTpro and carbamidomethylation of cysteine were set as static modifications, while methionine oxidation and asparagine/glutamine deamidation were set as variable modifications. A minimum peptide length of 7 and up to 2 miss cleavages were allowed. Peptide-spectrum matches (PSMs) were identified, quantified, and filtered to a 1% peptide false discovery rate (FDR) and then collapsed further to a final protein-level FDR of 1%. Proteins were quantified by summing reporter ion counts across all matching PSMs. Additionally, for *Vac14* mutants and controls, a minimum resolution filter was set at >40,000 and a minimum signal to noise (S:N) > 200 for analysis on the Astral device to ensure peaks above this ratio were used in quantitation. Briefly, a 0.003 Da (3 mDa) window around the theoretical m/z of each reporter ion was scanned and the maximum intensity nearest the theoretical m/z was used. Reporter ion intensities were adjusted to correct for the isotopic impurities of the different TMT reagents according to manufacturer specifications and adjusted to normalize ratios across labeling channels. Lastly, for each protein, signal-to-noise (S:N) measurements of the peptides were summed and then normalized to 100.

Differential protein abundance analysis between control and mutant was performed using a two-sample modified t-test implemented for quantitative proteomics data. Statistical significance was determined using false discovery rate (FDR) correction with an S0 parameter incorporated to balance fold-change magnitude and variance as previously described (Tusher et al., 2001). This generated adjusted *p*-values with the chosen 95% cutoff and Log_2(FoldChange) > 1 values for visualization in volcano plots and other analysis.

4.8. RNAseq

Mouse cortex was dissected and homogenized in Trizol using an 18 gauge needle followed by a 25 gauge needle. Total RNA was isolated using the column-based Qiagen RNeasy kit. Library prep was performed using 1 μg of input RNA with the Illumina Stranded Total RNA Prep Ligation with Ribo-Zero Plus kit. After depleting ribosomal RNA and performing cDNA synthesis, the DNA was quantitated using Qubit and equalized across samples. Illumina-compatible dual index primers were used during 15 PCR cycles. For experiments using isolated microglia as input, we followed a similar procedure but utilized less adaptor during library prep. The distribution of fragment sizes in cDNA libraries was analyzed using Tapestation. Libraries were The prepared libraries were subsequently sequencing using the Illumina NovaSeq X platform to generate 100 bp paired-end reads. Each sample was sequenced to a depth of at least 30 million reads. RNAseq libraries were aligned to mm10 using STAR v.2.7.9a (Dobin et al., 2013). Alignment files were then converted to bigwig format using deepTools (Ramírez et al., 2016) bamCoverage v.3.5.0. DESeq2 (Love et al., 2014) was then used to compute normalized reads and adjusted *p*-values. Browser snapshots were generated using karyoploteR (Gel and Serra, 2017). RNA-seq data generated in this study have been deposited in the BioProject/SRA data under accession code PRJNA1356645.

4.9. Gene ontology analysis

Genes related to significantly differential proteins or transcripts were entered into ShinyGO (Ge et al., 2020) version 0.77. All detected proteins in proteomics experiments were used as background. All detected transcripts in RNAseq experiments were used as background.

4.10. Immunoblot

Tissue homogenates (10%, weight/volume) were prepared by homogenization with a Polytron homogenizer in RIPA buffer (150 mM NaCl, 1% NP-40, 1% sodium deoxycholate, 0.1% SDS in 25 mM Tris, pH 7.5) containing complete EDTA-free protease inhibitor cocktail (Roche) and 1:1000 beta-mercaptoethanol. To generate supernatant and pellet fractions, lysates were centrifuged at 15,000 xg. The pellet was resuspended in RIPA buffer using the Polytron homogenizer. Protein was quantitated using the Bradford reagent. Electrophoresis on precast 4–20% SDS-PAGE gels (Criterion) occurred prior to transfer to Hybond nitrocellulose membranes (Amersham Biosciences). Membranes were pre-incubated for 1 h at room temperature in 3% BSA fraction V (Fischer Scientific) in TBST (Tris-buffered saline with Tween 20). Primary antibody incubation was carried out overnight at 4 degrees. Guinea pig anti-p62 (ARP American Research Products Cat# 03-GP62-C, RRID:AB_1542690) was used at 1:1000, rabbit anti-GFAP (Abcam Cat# ab7260, RRID:AB_305808) at 1:1000, mouse anti-GAPDH at 1:30,000 (Abcam Cat# ab9484, RRID:AB_307274), rabbit anti-Cathepsin D (Scripps laboratories, RC245) at 1:2000 and rabbit anti-p53 (Abcam Cat# ab131442, RRID:AB_11155283) at 1:500. Membranes were washed in TBST and incubated with peroxidase-labeled secondary antibodies for 1 h at room temp. Secondary antibodies were: donkey anti-guinea pig (Jackson ImmunoResearch Labs Cat# 706–035-148, RRID:AB_2340447), goat anti-rabbit (Jackson ImmunoResearch Labs Cat# 111–035-003, RRID:AB_2313567) and goat anti-mouse (Jackson ImmunoResearch Labs Cat# 115–035-003, RRID:AB_10015289). Chemiluminescence was detected with the Supersignal West Femto chemiluminescence reagent (Pierce) and Hybond-CL autoradiography film (Denville Scientific).

4.11. Fluorescence-activated cell sorting of microglia for RNA-seq

Microglia were isolated and labeled for ROS production as previously described (Mendiola et al., 2023). In brief, mice were perfused with phosphate buffered saline (PBS) and brains were extracted for single cell cell preparation. Tissues were incubated in lysis buffer (1 mg/mL collagenase D (Sigma-Aldrich), 0.05 mg/mL DNase1 (Sigma-Aldrich), 3

μM actinomycin D diluted in phosphate buffered saline with Ca^{2+} Mg^{2+} (Thermo Fisher Scientific) for 30 min at 37 °C. Myelin was depleted using a 37%/70% Percoll gradient with centrifugation setting 4 °C, 800 xg for 25 min. Cells were treated with Fc block in staining buffer (PBS supplemented with 0.2% bovine serum albumin) and 0.05 mM EDTA (Teknova), then incubated with primary antibodies for 30 min at 4 °C. The following primary antibodies from BioLegend were used at 1:200 dilution: CD11b (BioLegend Cat# 101207, RRID:AB_312790) and CD45 (BioLegend Cat# 103101, RRID:AB_312966). For intracellular ROS labeling, cells were incubated with 10 μM DCFDA in stain buffer for 30 min at 4 °C and directly analyzed by flow cytometry. Cells were incubated with 1 μM Sytox blue live/dead stain prior to analysis. For FACS of microglia, single live cells that expressed CD45lo/CD11b + were sorted into tubes containing RLT plus lysis buffer (Qiagen) supplemented with 1% 2-mercaptoethanol using a FACSMelody with BD FACSChorus. Approximately 40,000 microglia were collected per sample and lysates were frozen and stored at −80 °C until library preparation. Data analysis was performed with FlowJo v.10.10 software.

4.12. Paraffin embedding, immunohistochemistry

Brains from *Fig4* and *Vac14* global mutant mice were fixed overnight in 10% neutral buffered formalin at 4 °C. *Fig4* $^{f/f}$,Nes-cre mice were fixed at age P10. Each whole brain was dissected coronally into six pieces 200 μm apart and paraffin-embedded in a single block. Sections 5 μm in thickness were cut on a microtome and placed on adhesive hydrophilic glass slides (TOMO). Antibody detection was performed using an automated tissue immunostainer (Ventana Discovery Ultra, Ventana Medical Systems,Tucson, AZ, USA). Antigen retrieval was performed by incubating the slides in CC1 (tris-based; pH 8.5; Ventana) at 95 °C for 40 min for all epitopes except for p53 which used a total of 64 min of retrieval. Following retrieval, antibodies targeting p53 (1:1000, Leica Biosystems Cat# NCL-L-p53-CM5p, RRID:AB_2895247), Iba-1 (1:100, FUJIFILM Wako Pure Chemical Corporation Cat# 019–19741, RRID:AB_839504), ApoE (1:8000, Abcam Cat# ab183597, RRID:AB_3331650), CD11b (1:1000 Abcam Cat# ab133357, RRID:AB_2650514) and Fas (1:100, (Abcam Cat# ab271016, RRID:AB_3712731) were incubated on the tissue for 32 min at 37 °C. The secondary antibody (HRP-coupled goat anti-rabbit, Ventana OmniMap system, Roche Cat# 760–4815, RRID: AB_2811171) was incubated on the sections for 12 min at 37 °C. The primary antibody was visualized using DAB as a chromogen, followed by hematoxylin as a counterstain. Slides were rinsed in distilled water, dehydrated through ethanol and xylene, and coverslipped.

4.13. Analysis of immunohistochemistry

Slides were digitalized using the Zeiss AxioScan. Z1 Slide Scanner (Carl Zeiss Microscopy GmbH, Jena, Germany) at 20× magnification. For each specimen, the tissue piece with a clearly developed hippocampus (similar to hippocampal development between the 690–780 μm intervals shown in the coronal Allen Mouse Brain Atlas) was selected for image analysis. Quantification of p53 positive cell count was performed on FIJI using the "DAB IHC" macro in the automated image analysis pipeline "Andy's Algorithm" (Law et al., 2017). Image analysis optimizations were experimentally determined for different cohorts by changing the following parameters (threshold, size exclusion, and circularity exclusion). To determine the tissue area (pixels^2) of each scan, the upper and lower "Brightness" thresholds in the "Color Threshold" feature on FIJI were manually adjusted. Tissue area was converted from pixels^2 to mm^2. Manual positive cell count corrections for false positives (tissue artifacts or non-specific haze counted as positive cells) and false negatives (unambiguously dark cells exceeding size exclusion parameters) were performed with the aid of the "SlideJdemo2" macro in the "SlideJ" plugin (Della Mea et al., 2017), which split each whole slide scan into 40–60 tiles. Corresponding tiles from the original scan and positive overlay scan provided by Andy's Algorithm were compared. The numbers of positive cells per mm2 of tissue per animal, after manual corrections, were used for statistical analyses.

4.14. Measurement of lysosome glycosidase activity in brain

Ten percent homogenates of total brain were prepared in extraction buffer containing 0.25 M sucrose, 0.05 M tris pH 7.4 and 1 tablet of complete EDTA-free protease inhibitor cocktail (Roche) per 25 mL. Protein concentration was 1 mg/mL in the β-galactosidase and β-glucuronidase assays, and 0.5 mg/mL in β-hexosaminidase assays. Reactions were performed as previously described in 0.1 M citrate buffer pH 3.6 (β-galactosidase) or pH 4.6 (Felton et al., 1974). The para-nitrophenol substrates were used at a final concentration of 5 mM. The substrate for β-galactosidase was 2-nitrophenyl β-D-galactopyranoside (Sigma, N1127), for β-glucuronidase 4-nitrophenyl β-D-glucuronide (Sigma, N1627) and for β-hexosaminidase 4-nitrophenyl *N*-acetyl- β-D-glucosaminide (Sigma, N9376). Absorbance of p-nitrophenol was measured at 405 nm.

4.15. Quantification and statistical analysis

For details of the quantitative methods used in TMT proteomics and RNAseq, please refer to the Methods sections and Figure Legends. We used GraphPad Prism 10 software to perform other statistical tests described in Figure legends.

CRediT authorship contribution statement

Bridget Wong: Writing – review & editing, Writing – original draft, Visualization, Validation, Software, Methodology, Formal analysis, Data curation, Conceptualization. **Morgan Payne:** Visualization, Validation, Software, Methodology, Formal analysis, Data curation. **Alexander Silva:** Visualization, Validation, Methodology, Formal analysis, Data curation. **Emma Kurniawan:** Writing – review & editing, Methodology, Investigation. **Alison S. Eidman:** Visualization, Software, Methodology, Formal analysis, Data curation. **Donald Pizzo:** Visualization, Supervision, Software, Resources, Formal analysis. **Rachana Rajupalem:** Visualization, Software, Methodology, Formal analysis, Data curation. **Guy M. Lenk:** Supervision, Resources. **Joao A. Paulo:** Visualization, Validation, Supervision, Software, Resources, Methodology. **Taimur Khan:** Visualization, Software, Formal analysis. **Eeva-Liisa Eskelinen:** Writing – review & editing, Visualization, Supervision, Methodology, Investigation, Funding acquisition. **Steve P. Gygi:** Supervision, Software, Methodology, Funding acquisition. **Nicholas G. Brown:** Writing – review & editing, Visualization, Supervision, Software, Funding acquisition, Formal analysis. **Miriam H. Meisler:** Writing – review & editing, Supervision, Resources, Funding acquisition, Conceptualization. **Andrew S. Mendiola:** Writing – review & editing, Visualization, Supervision, Resources, Methodology, Funding acquisition, Formal analysis, Conceptualization. **Brandon M. Gassaway:** Writing – review & editing, Visualization, Validation, Supervision, Software, Resources, Methodology, Investigation, Funding acquisition, Formal analysis, Data curation, Conceptualization. **Cole J. Ferguson:** Writing – review & editing, Writing – original draft, Visualization, Validation, Supervision, Resources, Methodology, Investigation, Funding acquisition, Formal analysis, Data curation, Conceptualization.

Declaration of competing interest

The authors declare no competing interests.

Acknowledgments

We thank Chris Tracy at the BYU Biological Mass Spectrometry Facility for equipment access and technical assistance, and also thank the University of California, San Diego - Cellular and Molecular Medicine

Electron Microscopy Core (UCSD-CMM-EM Core, RRID:SCR_022039) and the Electron Microscopy Unit at Institute of Biotechnology, University of Helsinki, Finland. Members of the Ferguson, Mendiola and Gassaway labs provided helpful feedback on the study. Lois Weisman, Pilar Rivero-Rios and Tuna Uygun provided valuable critiques of this manuscript. V.L. Brandt assisted in the conceptualization and composition of this paper. This work was supported by NIH R01NS138924 (CJF), NIH R35GM128855 (NGB) and NIH R21NS139210 (CJF and NGB). MP is supported by funding from the BYU Simmons Center for Cancer Research.

Appendix A. Supplementary data

Supplementary data to this article can be found online at https://doi.org/10.1016/j.nbd.2026.107467.

Data availability

Data will be made available on request.

References

Abramson, J., Adler, J., Dunger, J., Evans, R., Green, T., Pritzel, A., Ronneberger, O., Willmore, L., Ballard, A.J., Bambrick, J., Bodenstein, S.W., Evans, D.A., Hung, C.-C., O'Neill, M., Reiman, D., Tunyasuvunakool, K., Wu, Z., Žemgulytė, A., Arvaniti, E., Beattie, C., Bertolli, O., Bridgland, A., Cherepanov, A., Congreve, M., Cowen-Rivers, A.I., Cowie, A., Figurnov, M., Fuchs, F.B., Gladman, H., Jain, R., Khan, Y.A., Low, C.M.R., Perlin, K., Potapenko, A., Savy, P., Singh, S., Stecula, A., Thillaisundaram, A., Tong, C., Yakneen, S., Zhong, E.D., Zielinski, M., Žídek, A., Bapst, V., Kohli, P., Jaderberg, M., Hassabis, D., Jumper, J.M., 2024. Accurate structure prediction of biomolecular interactions with AlphaFold 3. Nature 630, 493–500. https://doi.org/10.1038/s41586-024-07487-w.

Ai, Y., Meng, Y., Yan, B., Zhou, Q., Wang, X., 2024. The biochemical pathways of apoptotic, necroptotic, pyroptotic, and ferroptotic cell death. Mol. Cell 84, 170–179. https://doi.org/10.1016/j.molcel.2023.11.040.

Andersson-Rolf, A., Mustata, R.C., Merenda, A., Kim, J., Perera, S., Grego, T., Andrews, K., Tremble, K., Silva, J.C.R., Fink, J., Skarnes, W.C., Koo, B.-K., 2017. One-step generation of conditional and reversible gene knockouts. Nat. Methods 14, 287–289. https://doi.org/10.1038/nmeth.4156.

Angelova, P.R., Abramov, A.Y., 2018. Role of mitochondrial ROS in the brain: from physiology to neurodegeneration. FEBS Lett. 592, 692–702. https://doi.org/10.1002/1873-3468.12964.

Babcock, A.A., Kuziel, W.A., Rivest, S., Owens, T., 2003. Chemokine expression by glial cells directs leukocytes to sites of axonal injury in the CNS. J. Neurosci. 23, 7922–7930. https://doi.org/10.1523/JNEUROSCI.23-21-07922.2003.

Baulac, S., Lenk, G.M., Dufresnois, B., Ouled Amar Bencheikh, B., Couarch, P., Renard, J., Larson, P.A., Ferguson, C.J., Noé, E., Poirier, K., Hubans, C., Ferreira, S., Guerrini, R., Ouazzani, R., El Hachimi, K.H., Meisler, M.H., Leguern, E., 2014. Role of the phosphoinositide phosphatase *FIG 4* gene in familial epilepsy with polymicrogyria. Neurology 82, 1068–1075. https://doi.org/10.1212/WNL.0000000000000241.

Bolognin, S., Cozzi, B., Zambenedetti, P., Zatta, P., 2014. Metallothioneins and the central nervous system: from a deregulation in neurodegenerative diseases to the development of new therapeutic approaches. JAD 41, 29–42. https://doi.org/10.3233/JAD-130290.

Bose, S., De Heus, C., Kennedy, M.E., Wang, F., Jentsch, T.J., Klumperman, J., Stauber, T., 2023. Impaired autophagic clearance with a gain-of-function variant of the lysosomal cl−/H+ exchanger ClC-7. Biomolecules 13, 1799. https://doi.org/10.3390/biom13121799.

Brodeur, J., Thériault, C., Lessard-Beaudoin, M., Marcil, A., Dahan, S., Lavoie, C., 2012. LDLR-related protein 10 (LRP10) regulates amyloid precursor protein (APP) trafficking and processing: evidence for a role in Alzheimer's disease. Mol. Neurodegener. 7, 31. https://doi.org/10.1186/1750-1326-7-31.

Broz, P., Pelegrín, P., Shao, F., 2020. The gasdermins, a protein family executing cell death and inflammation. Nat. Rev. Immunol. 20, 143–157. https://doi.org/10.1038/s41577-019-0228-2.

Buechler, J., Salinas, P.C., 2018. Deficient Wnt Signaling and synaptic vulnerability in Alzheimer's disease: emerging roles for the LRP6 receptor. Front. Synaptic Neurosci. 10, 38. https://doi.org/10.3389/fnsyn.2018.00038.

Campeau, P.M., Lenk, G.M., Lu, J.T., Bae, Y., Burrage, L., Turnpenny, P., Román Corona-Rivera, J., Morandi, L., Mora, M., Reutter, H., Vulto-van Silfhout, A.T., Faivre, L., Haan, E., Gibbs, R.A., Meisler, M.H., Lee, B.H., 2013. Yunis-Varón syndrome is caused by mutations in FIG 4, encoding a phosphoinositide phosphatase. Am. J. Hum. Genet. 92, 781–791. https://doi.org/10.1016/j.ajhg.2013.03.020.

Cao, X., Lenk, G.M., Mikusevic, V., Mindell, J.A., Meisler, M.H., 2023. The chloride antiporter CLCN7 is a modifier of lysosome dysfunction in FIG 4 and VAC14 mutants. PLoS Genet. 19, e1010800. https://doi.org/10.1371/journal.pgen.1010800.

Cebrian, C., Loike, J.D., Sulzer, D., 2014. Neuronal MHC-I expression and its implications in synaptic function, axonal regeneration and Parkinson's and other brain diseases. Front. Neuroanat. 8. https://doi.org/10.3389/fnana.2014.00114.

Chebath, J., Benech, P., Revel, M., Vigneron, M., 1987. Constitutive expression of (2′–5′) oligo a synthetase confers resistance to picornavirus infection. Nature 330, 587–588. https://doi.org/10.1038/330587a0.

Chen, B.-H., Lin, Z.-Y., Zeng, X.-X., Jiang, Y.-H., Geng, F., 2024. LRP4-related signalling pathways and their regulatory role in neurological diseases. Brain Res. 1825, 148705. https://doi.org/10.1016/j.brainres.2023.148705.

Chen, Q., She, J., Zeng, W., Guo, J., Xu, H., Bai, X., Jiang, Y., 2017. Structure of mammalian endolysosomal TRPML1 channel in nanodiscs. Nature 550, 415–418. https://doi.org/10.1038/nature24035.

Chen, X., Firulyova, M., Manis, M., Herz, J., Smirnov, I., Aladyeva, E., Wang, C., Bao, X., Finn, M.B., Hu, H., Shchukina, I., Kim, M.W., Yuede, C.M., Kipnis, J., Artyomov, M. N., Ulrich, J.D., Holtzman, D.M., 2023. Microglia-mediated T cell infiltration drives neurodegeneration in tauopathy. Nature 615, 668–677. https://doi.org/10.1038/s41586-023-05788-0.

Chen, Y., Jin, H., Chen, J., Li, J., Găman, M.-A., Zou, Z., 2025. The multifaceted roles of apolipoprotein E4 in Alzheimer's disease pathology and potential therapeutic strategies. Cell Death Discov. 11, 312. https://doi.org/10.1038/s41420-025-02600-y.

Cherry, J.D., 2015. Arginase 1+ microglia reduce Aβ plaque deposition during IL-1β-dependent neuroinflammation. J. Neuroinflammation 12, 1–13.

Choi, C., Benveniste, E.N., 2004. Fas ligand/Fas system in the brain: regulator of immune and apoptotic responses. Brain Res. Rev. 44, 65–81. https://doi.org/10.1016/j.brainresrev.2003.08.007.

Chow, C.Y., Zhang, Y., Dowling, J.J., Jin, N., Adamska, M., Shiga, K., Szigeti, K., Shy, M. E., Li, J., Zhang, X., Lupski, J.R., Weisman, L.S., Meisler, M.H., 2007. Mutation of FIG 4 causes neurodegeneration in the pale tremor mouse and patients with CMT4J. Nature 448, 68–72. https://doi.org/10.1038/nature05876.

Chow, C.Y., Landers, J.E., Bergren, S.K., Sapp, P.C., Grant, A.E., Jones, J.M., Everett, L., Lenk, G.M., McKenna-Yasek, D.M., Weisman, L.S., Figlewicz, D., Brown, R.H., Meisler, M.H., 2009. Deleterious variants of FIG 4, a phosphoinositide phosphatase, in patients with ALS. Am. J. Hum. Genet. 84, 85–88. https://doi.org/10.1016/j.ajhg.2008.12.010.

Cuinat, S., Dubourg, C., Nicolas, G., De Sainte Agathe, J., Odent, S., Pasquier, L., Riou, A., 2025. Variants identified in a patient with Striatonigral degeneration and prolonged survival. Movement Disord. Clin. Pract. 12, 1668–1671. https://doi.org/10.1002/mdc3.70152.

Della Mea, V., Baroni, G.L., Pilutti, D., Di Loreto, C., 2017. SlideJ: an ImageJ plugin for automated processing of whole slide images. PloS One 12, e0180540. https://doi.org/10.1371/journal.pone.0180540.

Dobin, A., Davis, C.A., Schlesinger, F., Drenkow, J., Zaleski, C., Jha, S., Batut, P., Chaisson, M., Gingeras, T.R., 2013. STAR: ultrafast universal RNA-seq aligner. Bioinformatics 29, 15–21. https://doi.org/10.1093/bioinformatics/bts635.

Dokalis, N., Prinz, M., 2019. Resolution of neuroinflammation: mechanisms and potential therapeutic option. Semin. Immunopathol. 41, 699–709. https://doi.org/10.1007/s00281-019-00764-1.

Dong, X., Shen, D., Wang, X., Dawson, T., Li, X., Zhang, Q., Cheng, X., Zhang, Y., Weisman, L.S., Delling, M., Xu, H., 2010. PI(3,5)P2 controls membrane trafficking by direct activation of mucolipin Ca2+ release channels in the endolysosome. Nat. Commun. 1, 38. https://doi.org/10.1038/ncomms1037.

Dong, X.-P., Cheng, X., Mills, E., Delling, M., Wang, F., Kurz, T., Xu, H., 2008. The type IV mucolipidosis-associated protein TRPML1 is an endolysosomal iron release channel. Nature 455, 992–996. https://doi.org/10.1038/nature07311.

Elmer, B.M., McAllister, A.K., 2012. Major histocompatibility complex class I proteins in brain development and plasticity. Trends Neurosci. 35, 660–670. https://doi.org/10.1016/j.tins.2012.08.001.

Eng, J.K., Jahan, T.A., Hoopmann, M.R., 2013. Comet: an open-source MS / MS sequence database search tool. Proteomics 13, 22–24. https://doi.org/10.1002/pmic.201200439.

Fei, Y., Ding, Y., 2024. The role of ferroptosis in neurodegenerative diseases. Front. Cell. Neurosci. 18, 1475934. https://doi.org/10.3389/fncel.2024.1475934.

Felton, J., Meisler, M., Paigen, K., 1974. A locus determining β-galactosidase activity in the mouse. J. Biol. Chem. 249, 3267–3272. https://doi.org/10.1016/S0021-9258(19)42667-7.

Ferguson, C.J., Lenk, G.M., Meisler, M.H., 2009. Defective autophagy in neurons and astrocytes from mice deficient in PI(3,5)P2. Hum. Mol. Genet. 18, 4868–4878. https://doi.org/10.1093/hmg/ddp460.

Ferguson, C.J., Lenk, G.M., Meisler, M.H., 2010. PtdIns(3,5)P $_2$ and autophagy in mouse models of neurodegeneration. Autophagy 6, 170–171. https://doi.org/10.4161/auto.6.1.10626.

Ferguson, C.J., Lenk, G.M., Jones, J.M., Grant, A.E., Winters, J.J., Dowling, J.J., Giger, R. J., Meisler, M.H., 2012. Neuronal expression of fig 4 is both necessary and sufficient to prevent spongiform neurodegeneration. Hum. Mol. Genet. 21, 3525–3534. https://doi.org/10.1093/hmg/dds179.

Ferguson, C.J., Urso, O., Bodrug, T., Gassaway, B.M., Watson, E.R., Prabu, J.R., Lara-Gonzalez, P., Martinez-Chacin, R.C., Wu, D.Y., Brigatti, K.W., Puffenberger, E.G., Taylor, C.M., Haas-Givler, B., Jinks, R.N., Strauss, K.A., Desai, A., Gabel, H.W., Gygi, S.P., Schulman, B.A., Brown, N.G., Bonni, A., 2022. APC7 mediates ubiquitin signaling in constitutive heterochromatin in the developing mammalian brain. Mol. Cell 82, 90–105. https://doi.org/10.1016/j.molcel.2021.11.031.

Freeman, S.A., Uderhardt, S., Saric, A., Collins, R.F., Buckley, C.M., Mylvaganam, S., Boroumand, P., Plumb, J., Germain, R.N., Ren, D., Grinstein, S., 2020. Lipid-gated monovalent ion fluxes regulate endocytic traffic and support immune surveillance. Science 367, 301–305. https://doi.org/10.1126/science.aaw9544.

Gan, N., Han, Y., Zeng, W., Wang, Y., Xue, J., Jiang, Y., 2022. Structural mechanism of allosteric activation of TRPML1 by PI(3,5)P_2 and rapamycin. Proc. Natl. Acad. Sci. U. S. A. 119, e2120404119. https://doi.org/10.1073/pnas.2120404119.

Ge, S.X., Jung, D., Yao, R., 2020. ShinyGO: a graphical gene-set enrichment tool for animals and plants. Bioinformatics 36, 2628–2629. https://doi.org/10.1093/bioinformatics/btz931.

Gel, B., Serra, E., 2017. karyoploteR: an R/Bioconductor package to plot customizable genomes displaying arbitrary data. Bioinformatics 33, 3088–3090. https://doi.org/10.1093/bioinformatics/btx346.

Hasegawa, J., Strunk, B.S., Weisman, L.S., 2017. PI5P and PI(3,5)P_2: minor, but essential Phosphoinositides. Cell Struct. Funct. 42, 49–60. https://doi.org/10.1247/csf.17003.

Ho, C.Y., Alghamdi, T.A., Botelho, R.J., 2012. Phosphatidylinositol-3,5- *bis* phosphate: no longer the poor PIP_2. Traffic 13, 1–8. https://doi.org/10.1111/j.1600-0854.2011.01246.x.

Holemans, T., Sørensen, D.M., Van Veen, S., Martin, S., Hermans, D., Kemmer, G.C., Van Den Haute, C., Baekelandt, V., Günther Pomorski, T., Agostinis, P., Wuytack, F., Palmgren, M., Eggermont, J., Vangheluwe, P., 2015. A lipid switch unlocks Parkinson's disease-associated ATP13A2. Proc. Natl. Acad. Sci. U. S. A. 112, 9040–9045. https://doi.org/10.1073/pnas.1508220112.

Hong, S., Beja-Glasser, V.F., Nfonoyim, B.M., Frouin, A., Li, S., Ramakrishnan, S., Merry, K.M., Shi, Q., Rosenthal, A., Barres, B.A., Lemere, C.A., Selkoe, D.J., Stevens, B., 2016. Complement and microglia mediate early synapse loss in Alzheimer mouse models. Science 352, 712–716. https://doi.org/10.1126/science.aad8373.

Huang, Y., Liu, B., Sinha, S.C., Amin, S., Gan, L., 2023. Mechanism and therapeutic potential of targeting cGAS-STING signaling in neurological disorders. Mol. Neurodegeneration 18, 79. https://doi.org/10.1186/s13024-023-00672-x.

Jain, A., Zoncu, R., 2026. Lysosomes as hubs of metabolic sensing and cellular homeostasis. Mol. Cell 86, 533–552. https://doi.org/10.1016/j.molcel.2026.01.011.

Jefferies, C.A., 2019. Regulating IRFs in IFN driven disease. Front. Immunol. 10, 325. https://doi.org/10.3389/fimmu.2019.00325.

Jia, J., Claude-Taupin, A., Gu, Y., Choi, S.W., Peters, R., Bissa, B., Mudd, M.H., Allers, L., Pallikkuth, S., Lidke, K.A., Salemi, M., Phinney, B., Mari, M., Reggiori, F., Deretic, V., 2020. Galectin-3 coordinates a cellular system for lysosomal repair and removal. Dev. Cell 52, 69–87.e8. https://doi.org/10.1016/j.devcel.2019.10.025.

Jin, N., Chow, C.Y., Liu, L., Zolov, S.N., Bronson, R., Davisson, M., Petersen, J.L., Zhang, Y., Park, S., Duex, J.E., Goldowitz, D., Meisler, M.H., Weisman, L.S., 2008. VAC14 nucleates a protein complex essential for the acute interconversion of PI3P and PI(3,5)P2 in yeast and mouse. EMBO J. 27, 3221–3234. https://doi.org/10.1038/emboj.2008.248.

Kao, A.W., McKay, A., Singh, P.P., Brunet, A., Huang, E.J., 2017. Progranulin, lysosomal regulation and neurodegenerative disease. Nat. Rev. Neurosci. 18, 325–333. https://doi.org/10.1038/nrn.2017.36.

Karaoğlu, P., Köse, M., 2021. Expanding the spectrum of VAC14 related pediatric-onset neurological disease; striatonigral degeneration with brainstem involvement. Eur. J. Med. Genet. 64, 104117. https://doi.org/10.1016/j.ejmg.2020.104117.

Kodosaki, E., Bell, R., Sogorb-Esteve, A., Wiltshire, K., Zetterberg, H., Heslegrave, A., 2024. More than microglia: myeloid cells and biomarkers in neurodegeneration. Front. Neurosci. 18, 1499458. https://doi.org/10.3389/fnins.2024.1499458.

Kumar, V., 2019. Toll-like receptors in the pathogenesis of neuroinflammation. J. Neuroimmunol. 332, 16–30. https://doi.org/10.1016/j.jneuroim.2019.03.012.

Kutchukian, C., Casas, M., Dixon, R.E., Dickson, E.J., 2025. Disruption of the PIKfyve complex unveils an adaptive mechanism to promote lysosomal repair and mitochondrial homeostasis. Nat. Commun. 16, 10761. https://doi.org/10.1038/s41467-025-65798-6.

Law, A.M.K., Yin, J.X.M., Castillo, L., Young, A.I.J., Piggin, C., Rogers, S., Caldon, C.E., Burgess, A., Millar, E.K.A., O'Toole, S.A., Gallego-Ortega, D., Ormandy, C.J., Oakes, S.R., 2017. Andy's algorithms: new automated digital image analysis pipelines for FIJI. Sci. Rep. 7, 15717. https://doi.org/10.1038/s41598-017-15885-6.

Lawrence, R.E., Zoncu, R., 2019. The lysosome as a cellular Centre for signalling, metabolism and quality control. Nat. Cell Biol. 21, 133–142. https://doi.org/10.1038/s41556-018-0244-7.

Ledvin, L., Gassaway, B.M., Tawil, J., Urso, O., Pizzo, D., Welsh, K.A., Bolhuis, D.L., Fisher, D., Bonni, A., Gygi, S.P., Brown, N.G., Ferguson, C.J., 2023. The anaphase-promoting complex controls a ubiquitination-phosphoprotein axis in chromatin during neurodevelopment. Dev. Cell 58, 2666–2683.e9. https://doi.org/10.1016/j.devcel.2023.10.002.

Lees, J.A., Li, P., Kumar, N., Weisman, L.S., Reinisch, K.M., 2020. Insights into lysosomal PI(3,5)P2 homeostasis from a structural-biochemical analysis of the PIKfyve lipid kinase complex. Mol. Cell 80, 736–743.e4. https://doi.org/10.1016/j.molcel.2020.10.003.

Lenk, G.M., Ferguson, C.J., Chow, C.Y., Jin, N., Jones, J.M., Grant, A.E., Zolov, S.N., Winters, J.J., Giger, R.J., Dowling, J.J., Weisman, L.S., Meisler, M.H., 2011. Pathogenic mechanism of the FIG 4 mutation responsible for charcot-marie-tooth disease CMT4J. PLoS Genet. 7. https://doi.org/10.1371/journal.pgen.1002104.

Lenk, G.M., Szymanska, K., Debska-Vielhaber, G., Rydzanicz, M., Walczak, A., Bekiesinska-Figatowska, M., Vielhaber, S., Hallmann, K., Stawinski, P., Buehring, S., Hsu, D.A., Kunz, W.S., Meisler, M.H., Ploski, R., 2016. Biallelic mutations of VAC14 in Pediatric-onset neurological disease. Am. J. Hum. Genet. 99, 188–194. https://doi.org/10.1016/j.ajhg.2016.05.008.

Leray, X., Hilton, J.K., Nwangwu, K., Becerril, A., Mikusevic, V., Fitzgerald, G., Amin, A., Weston, M.R., Mindell, J.A., 2022. Tonic inhibition of the chloride/proton antiporter ClC-7 by PI(3,5)P2 is crucial for lysosomal pH maintenance. eLife 11, e74136. https://doi.org/10.7554/eLife.74136.

Lewandowski, D., Konieczny, M., Różycka, A., Chrzanowski, K., Owecki, W., Kalinowski, J., Stepura, M., Jagodziński, P., Dorszewska, J., 2025. Cathepsins in neurological diseases. Int. J. Mol. Sci. 26, 7886. https://doi.org/10.3390/ijms26167886.

Liu, C.-Y., Lin, J.-L., Feng, S.-Y., Che, C.-H., Huang, H.-P., Zou, Z.-Y., 2022. Novel variants in the *FIG 4* gene associated with Chinese sporadic amyotrophic lateral sclerosis with slow progression. J. Clin. Neurol. 18, 41. https://doi.org/10.3988/jcn.2022.18.1.41.

Liu, F.-T., Stowell, S.R., 2023. The role of galectins in immunity and infection. Nat. Rev. Immunol. 23, 479–494. https://doi.org/10.1038/s41577-022-00829-7.

Love, M.I., Huber, W., Anders, S., 2014. Moderated estimation of fold change and dispersion for RNA-seq data with DESeq2. Genome Biol. 15, 550. https://doi.org/10.1186/s13059-014-0550-8.

Mendiola, A.S., Ryu, J.K., Bardehle, S., Meyer-Franke, A., Ang, K.K.-H., Wilson, C., Baeten, K.M., Hanspers, K., Merlini, M., Thomas, S., Petersen, M.A., Williams, A., Thomas, R., Rafalski, V.A., Meza-Acevedo, R., Tognatta, R., Yan, Z., Pfaff, S.J., Machado, M.R., Bedard, C., Rios Coronado, P.E., Jiang, X., Wang, J., Pleiss, M.A., Green, A.J., Zamvil, S.S., Pico, A.R., Bruneau, B.G., Arkin, M.R., Akassoglou, K., 2020. Transcriptional profiling and therapeutic targeting of oxidative stress in neuroinflammation. Nat. Immunol. 21, 513–524. https://doi.org/10.1038/s41590-020-0654-0.

Mendiola, A.S., Yan, Z., Dixit, K., Johnson, J.R., Bouhaddou, M., Meyer-Franke, A., Shin, M.-G., Yong, Y., Agrawal, A., MacDonald, E., Muthukumar, G., Pearce, C., Arun, N., Cabriga, B., Meza-Acevedo, R., Alzamora, M.D.P.S., Zamvil, S.S., Pico, A. R., Ryu, J.K., Krogan, N.J., Akassoglou, K., 2023. Defining blood-induced microglia functions in neurodegeneration through multiomic profiling. Nat. Immunol. 24, 1173–1187. https://doi.org/10.1038/s41590-023-01522-0.

Miller, F.D., Pozniak, C.D., Walsh, G.S., 2000. Neuronal life and death: an essential role for the p53 family. Cell Death Differ. 7, 880–888. https://doi.org/10.1038/sj.cdd.4400736.

Mitroshina, E.V., Saviuk, M., Vedunova, M.V., 2023. Necroptosis in CNS diseases: focus on astrocytes. Front. Aging Neurosci. 14, 1016053. https://doi.org/10.3389/fnagi.2022.1016053.

Müller, M., Carter, S., Hofer, M.J., Campbell, I.L., 2010. Review: the chemokine receptor CXCR3 and its ligands CXCL9, CXCL10 and CXCL11 in neuroimmunity - a tale of conflict and conundrum: CXCR3 and its ligands in CNS inflammation. Neuropathol. Appl. Neurobiol. 36, 368–387. https://doi.org/10.1111/j.1365-2990.2010.01089.x.

Murata, S., Takahama, Y., Kasahara, M., Tanaka, K., 2018. The immunoproteasome and thymoproteasome: functions, evolution and human disease. Nat. Immunol. 19, 923–931. https://doi.org/10.1038/s41590-018-0186-z.

Nakamura, S., Shimazawa, M., Hara, H., 2018. Physiological roles of Metallothioneins in central nervous system diseases. Biol. Pharm. Bull. 41, 1006–1013. https://doi.org/10.1248/bpb.b17-00856.

Nakanishi, H., Wu, Z., 2009. Microglia-aging: roles of microglial lysosome- and mitochondria-derived reactive oxygen species in brain aging. Behav. Brain Res. 201, 1–7. https://doi.org/10.1016/j.bbr.2009.02.001.

Nardo, G., Trolese, M.C., Bendotti, C., 2016. Major histocompatibility complex I expression by motor neurons and its implication in amyotrophic lateral sclerosis. Front. Neurol. 7. https://doi.org/10.3389/fneur.2016.00089.

Navarrete-Perea, J., Yu, Q., Gygi, S.P., Paulo, J.A., 2018. Streamlined tandem mass tag (SL-TMT) protocol: an efficient strategy for quantitative (Phospho)proteome profiling using tandem mass tag-synchronous precursor selection-MS3. J. Proteome Res. 17, 2226–2236. https://doi.org/10.1021/acs.jproteome.8b00217.

Nicholson, G., Lenk, G.M., Reddel, S.W., Grant, A.E., Towne, C.F., Ferguson, C.J., Simpson, E., Scheuerle, A., Yasick, M., Hoffman, S., Blouin, R., Brandt, C., Coppola, G., Biesecker, L.G., Batish, S.D., Meisler, M.H., 2011. Distinctive genetic and clinical features of CMT4J: a severe neuropathy caused by mutations in the PI(3,5)P2 phosphatase FIG 4. Brain 134, 1959–1971. https://doi.org/10.1093/brain/awr148.

Nicoli, E.-R., Weston, M.R., Hackbarth, M., Becerril, A., Larson, A., Zein, W.M., Baker, P. R., Burke, J.D., Dorward, H., Davids, M., Huang, Yan, Adams, D.R., Zerfas, P.M., Chen, D., Markello, T.C., Toro, C., Wood, T., Elliott, G., Vu, M., Acosta, M.T., Adams, D.R., Agrawal, P., Alejandro, M.E., Allard, P., Alvey, J., Andrews, A., Ashley, E.A., Azamian, M.S., Bacino, C.A., Bademci, G., Baker, E., Balasubramanyam, A., Baldridge, D., Bale, J., Barbouth, D., Batzli, G.F., Bayrak-Toydemir, P., Beggs, A.H., Bejerano, G., Bellen, H.J., Bernstein, J.A., Berry, G.T., Bican, A., Bick, D.P., Birch, C.L., Bivona, S., Bohnsack, J., Bonnenmann, C., Bonner, D., Boone, B.E., Bostwick, B.L., Botto, L., Briere, L.C., Brokamp, E., Brown, D.M., Brush, M., Burke, E.A., Burrage, L.C., Butte, M.J., Carey, J., Carrasquillo, O., Chang, T.C.P., Chao, H.-T., Clark, G.D., Coakley, T.R., Cobban, L.A., Cogan, J.D., Cole, F.S., Colley, H.A., Cooper, C.M., Cope, H., Craigen, W.J., D'Souza, P., Dasari, S., Davids, M., Dayal, J.G., Dell'Angelica, E.C., Dhar, S.U., Dorrani, N., Dorset, D.C., Douine, E.D., Draper, D.D., Duncan, L., Eckstein, D.J., Emrick, L.T., Eng, C.M., Esteves, C., Estwick, T., Fernandez, L., Ferreira, C., Fieg, E. L., Fisher, P.G., Fogel, B.L., Forghani, I., Fresard, L., Gahl, W.A., Godfrey, R.A., Goldman, A.M., Goldstein, D.B., Gourdine, J.-P.F., Grajewski, A., Groden, C.A., Gropman, A.L., Haendel, M., Hamid, R., Hanchard, N.A., Hayes, N., High, F., Holm, I.A., Hom, J., Huang, A., Huang, Yong, Isasi, R., Jamal, F., Jiang, Y., Johnston, J.M., Jones, A.L., Karaviti, L., Kelley, E.G., Kiley, D., Koeller, D.M., Kohane, I.S., Kohler, J.N., Krakow, D., Krasnewich, D.M., Korrick, S., Koziura, M., Krier, J.B., Kyle, J.E., Lalani, S.R., Lam, B., Lanpher, B.C., Lanza, I.R., Lau, C.C., Lazar, J., LeBlanc, K., Lee, B.H., Lee, H., Levitt, R., Levy, S.E., Lewis, R.A., Lincoln, S. A., Liu, P., Liu, X.Z., Longo, N., Loo, S.K., Loscalzo, J., Maas, R.L., Macnamara, E.F., MacRae, C.A., Maduro, V.V., Majcherska, M.M., Malicdan, M.C.V., Mamounas, L.A., Manolio, T.A., Mao, R., Markello, T.C., Marom, R., Marth, G., Martin, B.A., Martin, M.G., Martínez-Agosto, J.A., Marwaha, S., May, T., McCauley, J., McConkie-

Rosell, A., McCormack, C.E., McCray, A.T., Metz, T.O., Might, M., Morava-Kozicz, E., Moretti, P.M., Morimoto, M., Mulvihill, J.J., Murdock, D.R., Nath, A., Nelson, S.F., Newberry, J.S., Newman, J.H., Nicholas, S.K., Novacic, D., Oglesbee, D., Orengo, J. P., Pace, L., Pak, S., Pallais, J.C., Palmer, C.G.S., Papp, J.C., Parker, N.H., Phillips, J. A., Posey, J.E., Postlethwait, J.H., Potocki, L., Pusey, B.N., Quinlan, A., Raja, A.N., Renteria, G., Reuter, C.M., Rives, L., Robertson, A.K., Rodan, L.H., Rosenfeld, J.A., Rowley, R.K., Ruzhnikov, M., Sacco, R., Sampson, J.B., Samson, S.L., Saporta, M., Schaechter, J., Schedl, T., Schoch, K., Scott, D.A., Shakachite, L., Sharma, P., Shashi, V., Shields, K., Shin, J., Signer, R., Sillari, C.H., Silverman, E.K., Sinsheimer, J.S., Sisco, K., Smith, K.S., Solnica-Krezel, L., Spillmann, R.C., Stoler, J. M., Stong, N., Sullivan, J.A., Sutton, S., Sweetser, D.A., Tabor, H.K., Tamburro, C.P., Tan, Q.K.-G., Tekin, M., Telischi, F., Thorson, W., Tifft, C.J., Toro, C., Tran, A.A., Urv, T.K., Velinder, M., Viskochil, D., Vogel, T.P., Wahl, C.E., Walley, N.M., Walsh, C.A., Walker, M., Wambach, J., Wan, J., Wang, L., Wangler, M.F., Ward, P.A., Waters, K.M., Webb-Robertson, B.-J.M., Wegner, D., Westerfield, M., Wheeler, M.T., Wise, A.L., Wolfe, L.A., Woods, J.D., Worthey, E.A., Yamamoto, S., Yang, J., Yoon, A. J., Yu, G., Zastrow, D.B., Zhao, C., Zuchner, S., Zheng, W., Garrett, L.J., Tifft, C.J., Gahl, W.A., Day-Salvatore, D.L., Mindell, J.A., Malicdan, M.C.V., 2019. Lysosomal storage and albinism due to effects of a De novo CLCN7 variant on lysosomal acidification. Am. J. Human Genet. 104, 1127–1138. https://doi.org/10.1016/j.ajhg.2019.04.008.

Nixon, R.A., Rubinsztein, D., 2024. Mechanisms of autophagy–lysosome dysfunction in neurodegenerative diseases. Nat. Rev. Mol. Cell Biol. 25, 926–946.

Ofengeim, D., Mazzitelli, S., Ito, Y., DeWitt, J.P., Mifflin, L., Zou, C., Das, S., Adiconis, X., Chen, H., Zhu, H., Kelliher, M.A., Levin, J.Z., Yuan, J., 2017. RIPK1 mediates a disease-associated microglial response in Alzheimer's disease. Proc. Natl. Acad. Sci. U. S. A. 114. https://doi.org/10.1073/pnas.1714175114.

Paul, B.D., Snyder, S.H., Bohr, V.A., 2021. Signaling by cGAS–STING in neurodegeneration, neuroinflammation, and aging. Trends Neurosci. 44, 83–96. https://doi.org/10.1016/j.tins.2020.10.008.

Pedersen, M.Ø., Jensen, R., Pedersen, D.S., Skjolding, A.D., Hempel, C., Maretty, L., Penkowa, M., 2009. Metallothionein-I+II in neuroprotection. BioFactors 35, 315–325. https://doi.org/10.1002/biof.44.

Perez-Riverol, Y., Csordas, A., Bai, J., Bernal-Llinares, M., Hewapathirana, S., Kundu, D. J., Inuganti, A., Griss, J., Mayer, G., Eisenacher, M., Pérez, E., Uszkoreit, J., Pfeuffer, J., Sachsenberg, T., Yılmaz, Ş., Tiwary, S., Cox, J., Audain, E., Walzer, M., Jarnuczak, A.F., Ternent, T., Brazma, A., Vizcaíno, J.A., 2019. The PRIDE database and related tools and resources in 2019: improving support for quantification data. Nucleic Acids Res. 47, D442–D450. https://doi.org/10.1093/nar/gky1106.

Pottier, C., Zhou, X., Perkerson, R.B., Baker, M., Jenkins, G.D., Serie, D.J., Ghidoni, R., Benussi, L., Binetti, G., López De Munain, A., Zulaica, M., Moreno, F., Le Ber, I., Pasquier, F., Hannequin, D., Sánchez-Valle, R., Antonell, A., Lladó, A., Parsons, T.M., Finch, N.A., Finger, E.C., Lippa, C.F., Huey, E.D., Neumann, M., Heutink, P., Synofzik, M., Wilke, C., Rissman, R.A., Slawek, J., Sitek, E., Johannsen, P., Nielsen, J. E., Ren, Y., Van Blitterswijk, M., DeJesus-Hernandez, M., Christopher, E., Murray, M. E., Bieniek, K.F., Evers, B.M., Ferrari, C., Rollinson, S., Richardson, A., Scarpini, E., Fumagalli, G.G., Padovani, A., Hardy, J., Momeni, P., Ferrari, R., Frangipane, F., Maletta, R., Anfossi, M., Gallo, M., Petrucelli, L., Suh, E., Lopez, O.L., Wong, T.H., Van Rooij, J.G.J., Seelaar, H., Mead, S., Caselli, R.J., Reiman, E.M., Noel Sabbagh, M., Kjolby, M., Nykjaer, A., Karydas, A.M., Boxer, A.L., Grinberg, L.T., Grafman, J., Spina, S., Oblak, A., Mesulam, M.-M., Weintraub, S., Geula, C., Hodges, J.R., Piguet, O., Brooks, W.S., Irwin, D.J., Trojanowski, J.Q., Lee, E.B., Josephs, K.A., Parisi, J.E., Ertekin-Taner, N., Knopman, D.S., Nacmias, B., Piaceri, I., Bagnoli, S., Sorbi, S., Gearing, M., Glass, J., Beach, T.G., Black, S.E., Masellis, M., Rogaeva, E., Vonsattel, J.-P., Honig, L.S., Kofler, J., Bruni, A.C., Snowden, J., Mann, D., Pickering-Brown, S., Diehl-Schmid, J., Winkelmann, J., Galimberti, D., Graff, C., Öijerstedt, L., Troakes, C., Al-Sarraj, S., Cruchaga, C., Cairns, N.J., Rohrer, J.D., Halliday, G.M., Kwok, J.B., Van Swieten, J.C., White, C.L., Ghetti, B., Murell, J.R., Mackenzie, I.R.A., Hsiung, G.-Y.R., Borroni, B., Rossi, G., Tagliavini, F., Wszolek, Z.K., Petersen, R.C., Bigio, E.H., Grossman, M., Van Deerlin, V.M., Seeley, W.W., Miller, B.L., Graff-Radford, N.R., Boeve, B.F., Dickson, D.W., Biernacka, J.M., Rademakers, R., 2018. Potential genetic modifiers of disease risk and age at onset in patients with frontotemporal lobar degeneration and GRN mutations: a genome-wide association study. Lancet Neurol. 17, 548–558. https://doi.org/10.1016/S1474-4422(18)30126-1.

Quadri, M., Mandemakers, W., Grochowska, M.M., Masius, R., Geut, H., Fabrizio, E., Breedveld, G.J., Kuipers, D., Minneboo, M., Vergouw, L.J.M., Carreras Mascaro, A., Yonova-Doing, E., Simons, E., Zhao, T., Di Fonzo, A.B., Chang, H.-C., Parchi, P., Melis, Marta, Correia Guedes, L., Criscuolo, C., Thomas, A., Brouwer, R.W.W., Heijsman, D., Ingrassia, A.M.T., Calandra Buonaura, G., Rood, J.P., Capellari, S., Rozemuller, A.J., Sarchioto, M., Fen Chien, H., Vanacore, N., Olgiati, S., Wu-Chou, Y.-H., Yeh, T.-H., Boon, A.J.W., Hoogers, S.E., Ghazvini, M., IJpma, A.S., Van IJcken, W.F.J., Onofrj, M., Barone, P., Nicholl, D.J., Puschmann, A., De Mari, M., Kievit, A.J., Barbosa, E., De Michele, G., Majoor-Krakauer, D., Van Swieten, J.C., De Jong, F.J., Ferreira, J.J., Cossu, Giovanni, Lu, C.-S., Meco, G., Cortelli, P., Van De Berg, W.D.J., Bonifati, V., Bonifati, V., Quadri, M., Mandemakers, W., Kievit, A.J.A., Boon, A.J.W., Rood, J.P.A., Vergouw, L.J.M., De Jong, F.J., Van Swieten, J.C., Mattace-Raso, F.U.S., Leenders, K.L., Ferreira, J.J., Correia Guedes, L., Puschmann, A., Ygland, E., Nilsson, C., Chien, H.F., Barbosa, E., Bannach Jardim, L., Rieder, C.R.M., Chang, H.-C., Lu, C.-S., Wu-Chou, Y.-H., Yeh, T.-H., Lopiano, L., Tassorelli, C., Pacchetti, C., Riboldazzi, G., Bono, G., Comi, C., Padovani, A., Borroni, B., Raudino, F., Fincati, E., Tinazzi, M., Bonizzato, A., Ferracci, C., Dalla Libera, A., Abbruzzese, G., Cortelli, P., Capellari, S., Marconi, R., Guidi, M., Onofrj, M., Thomas, A., Vanacore, N., Meco, G., Fabrizio, E., Fabbrini, G., Berardelli, A., Stocchi, F., Vacca, L., Barone, P., Picillo, M., De Michele, G., Criscuolo, C., De Mari, M., Dell'Aquila, C., Iliceto, G., Toni, V., Trianni, G., Gagliardi, M., Annesi, G., Quattrone, A., Saddi, V., Cossu, Gianni, Melis, Maurizio, 2018. LRP10 genetic variants in familial Parkinson's disease and dementia with Lewy bodies: a genome-wide linkage and sequencing study. Lancet Neurol. 17, 597–608. https://doi.org/10.1016/S1474-4422(18)30179-0.

Quick, J.D., Silva, C., Wong, J.H., Lim, K.L., Reynolds, R., Barron, A.M., Zeng, J., Lo, C. H., 2023. Lysosomal acidification dysfunction in microglia: an emerging pathogenic mechanism of neuroinflammation and neurodegeneration. J. Neuroinflammation 20, 185. https://doi.org/10.1186/s12974-023-02866-y.

Ramírez, F., Ryan, D.P., Grüning, B., Bhardwaj, V., Kilpert, F., Richter, A.S., Heyne, S., Dündar, F., Manke, T., 2016. deepTools2: a next generation web server for deep-sequencing data analysis. Nucleic Acids Res. 44, W160–W165. https://doi.org/10.1093/nar/gkw257.

Reho, P., Koga, S., Shah, Z., Chia, R., the International LBD Genomics Consortium, The American Genome Center, Rademakers, R., Dalgard, C.L., Boeve, B.F., Beach, T.G., Dickson, D.W., Ross, O.A., Scholz, S.W., 2022. GRN mutations are associated with Lewy body dementia. Mov. Disord. 37, 1943–1948. https://doi.org/10.1002/mds.29144.

Rivero-Ríos, P., Weisman, L.S., 2022. Roles of PIKfyve in multiple cellular pathways. Curr. Opin. Cell Biol. 76, 102086. https://doi.org/10.1016/j.ceb.2022.102086.

Root, J., Merino, P., Nuckols, A., Johnson, M., Kukar, T., 2021. Lysosome dysfunction as a cause of neurodegenerative diseases: lessons from frontotemporal dementia and amyotrophic lateral sclerosis. Neurobiol. Dis. 154, 105360. https://doi.org/10.1016/j.nbd.2021.105360.

Scott, O., Saran, E., Freeman, S.A., 2025. The spectrum of lysosomal stress and damage responses: from mechanosensing to inflammation. EMBO Rep. 26, 1425–1439. https://doi.org/10.1038/s44319-025-00405-9.

She, H., Zheng, J., Zhao, G., Du, Y., Tan, L., Chen, Z.-S., Wu, Y., Li, Y., Liu, Y., Sun, Y., Hu, Y., Zuo, D., Mao, Q., Liu, L., Li, T., 2025. Arginase 1 drives mitochondrial cristae remodeling and PANoptosis in ischemia/hypoxia-induced vascular dysfunction. Sig. Transduct. Target Ther. 10, 167. https://doi.org/10.1038/s41392-025-02255-2.

She, J., Guo, J., Chen, Q., Zeng, W., Jiang, Y., Bai, X., 2018. Structural insights into the voltage and phospholipid activation of the mammalian TPC1 channel. Nature 556, 130–134. https://doi.org/10.1038/nature26139.

Shi, F.-D., Yong, V.W., 2025. Neuroinflammation across neurological diseases. Science 388, eadx0043. https://doi.org/10.1126/science.adx0043.

Sidransky, E., Nalls, M.A., Aasly, J.O., Aharon-Peretz, J., Annesi, G., Barbosa, E.R., Bar-Shira, A., Berg, D., Bras, J., Brice, A., Marco, E.V.D., Dürr, A., Eblan, M.J., Fahn, S., Farrer, M.J., Gan-Or, Z., Gasser, T., Gershoni-Baruch, R., Giladi, N., Griffith, A., Gurevich, T., Januario, C., Kropp, P., Lang, A.E., Mirelman, A., Mitsui, J., Mizuta, I., Nicoletti, G., Oliveira, C., Ottman, R., Orr-Urtreger, A., Pereira, L.V., Quattrone, A., Rogaeva, E., Rolfs, A., Rosenbaum, H., Rozenberg, R., Samii, A., Samaddar, T., Schulte, C., Sharma, M., Singleton, A., Spitz, M., Wolfsberg, T.G., 2009. Multicenter analysis of glucocerebrosidase mutations in parkinson's disease. New England J. Med. 361, 1651–1661.

Stratoulias, V., Ruiz, R., Kanatani, S., Osman, A.M., Keane, L., Armengol, J.A., Rodríguez-Moreno, A., Murgoci, A.-N., García-Domínguez, I., Alonso-Bellido, I., González Ibáñez, F., Picard, K., Vázquez-Cabrera, G., Posada-Pérez, M., Vernoux, N., Tejera, D., Grabert, K., Cheray, M., González-Rodríguez, P., Pérez-Villegas, E.M., Martínez-Gallego, I., Lastra-Romero, A., Brodin, D., Avila-Cariño, J., Cao, Y., Airavaara, M., Uhlén, P., Heneka, M.T., Tremblay, M.-È., Blomgren, K., Venero, J.L., Joseph, B., 2023. ARG1-expressing microglia show a distinct molecular signature and modulate postnatal development and function of the mouse brain. Nat. Neurosci. 26, 1008–1020. https://doi.org/10.1038/s41593-023-01326-3.

Strunk, B.S., Steinfeld, N., Lee, S., Jin, N., Muñoz-Rivera, C., Meeks, G., Thomas, A., Akemann, C., Mapp, A.K., MacGurn, J.A., Weisman, L.S., 2020. Roles for a lipid phosphatase in the activation of its opposing lipid kinase. MBoC 31, 1835–1845. https://doi.org/10.1091/mbc.E18-09-0556.

Tan, J.X., Lv, B., Li, J., Li, T., Du, F., Chen, X., Zhang, X., Bai, X., Chen, Z.J., 2026. PtdIns(3,5)P2 is an endogenous ligand of STING in innate immune signalling. Nature. https://doi.org/10.1038/s41586-025-10084-0.

Tronche, F., Kellendonk, C., Kretz, O., Gass, P., Anlag, K., Orban, P.C., Bock, R., Klein, R., Schütz, G., 1999. Disruption of the glucocorticoid receptor gene in the nervous system results in reduced anxiety. Nat. Genet. 23, 99–103. https://doi.org/10.1038/12703.

Tusher, V.G., Tibshirani, R., Chu, G., 2001. Significance analysis of microarrays applied to the ionizing radiation response. Proc. Natl. Acad. Sci. U. S. A. 98, 5116–5121. https://doi.org/10.1073/pnas.091062498.

Udayar, V., Chen, Y., Sidransky, E., Jagasia, R., 2022. Lysosomal dysfunction in neurodegeneration: emerging concepts and methods. Trends Neurosci. 45, 184–199. https://doi.org/10.1016/j.tins.2021.12.004.

Van Der Lienden, M.J.C., Gaspar, P., Boot, R., Aerts, J.M.F.G., Van Eijk, M., 2018. Glycoprotein non-metastatic protein B: an emerging biomarker for lysosomal dysfunction in macrophages. IJMS 20, 66. https://doi.org/10.3390/ijms20010066.

Wallings, R.L., Humble, S.W., Ward, M.E., Wade-Martins, R., 2019. Lysosomal dysfunction at the Centre of Parkinson's disease and frontotemporal dementia/amyotrophic lateral sclerosis. Trends Neurosci. 42, 899–912. https://doi.org/10.1016/j.tins.2019.10.002.

Wang, X., Zhang, X., Dong, X., Samie, M., Li, X., Cheng, X., Goschka, A., Shen, D., Zhou, Y., Harlow, J., Zhu, M.X., Clapham, D.E., Ren, D., Xu, H., 2012. TPC proteins are phosphoinositide- activated sodium-selective ion channels in endosomes and lysosomes. Cell 151, 372–383. https://doi.org/10.1016/j.cell.2012.08.036.

Winters, J.J., Ferguson, C.J., Lenk, G.M., Giger-Mateeva, V.I., Shrager, P., Meisler, M.H., Giger, R.J., 2011. Congenital CNS hypomyelination in the *fig 4* null mouse is rescued by neuronal expression of the PI(3,5)P $_2$ phosphatase *fig 4*. J. Neurosci. 31, 17736–17751. https://doi.org/10.1523/JNEUROSCI.1482-11.2011.

Woo, M.S., Brand, J., Bal, L.C., Moritz, M., Walkenhorst, M., Vieira, V., Ipenberg, I., Rothammer, N., Wang, M., Dogan, B., Loreth, D., Mayer, C., Nagel, D., Wagner, I., Pfeffer, L.K., Landgraf, P., Van Ham, M., Mattern, K.M.-J., Winschel, I., Frantz, N., Sonner, J.K., Grosshans, H.K., Miguela, A., Bauer, S., Meurs, N., Müller, A., Binkle-Ladisch, L., Salinas, G., Jänsch, L., Dieterich, D.C., Riedner, M., Krüger, E., Heppner, F.L., Glatzel, M., Puelles, V.G., Engler, J.B., Nyengaard, J.R., Misgeld, T., Kerschensteiner, M., Merkler, D., Meyer-Schwesinger, C., Friese, M.A., 2025. The immunoproteasome disturbs neuronal metabolism and drives neurodegeneration in multiple sclerosis. Cell 188, 4567–4585.e32. https://doi.org/10.1016/j.cell.2025.05.029.

Yu, C.-E., Bird, T.D., Bekris, L.M., Montine, T.J., Leverenz, J.B., Steinbart, E., Galloway, N.M., Feldman, H., Woltjer, R., Miller, C.A., Wood, E.M., Grossman, M., McCluskey, L., Clark, C.M., Neumann, M., Danek, A., Galasko, D.R., Arnold, S.E., Chen-Plotkin, A., Karydas, A., Miller, B.L., Trojanowski, J.Q., Lee, V.M.-Y., Schellenberg, G.D., Van Deerlin, V.M., 2010. The Spectrum of mutations in progranulin: a collaborative study screening 545 cases of neurodegeneration. Arch. Neurol. 67. https://doi.org/10.1001/archneurol.2009.328.

Zamanian, J.L., Xu, L., Foo, L.C., Nouri, N., Zhou, L., Giffard, R.G., Barres, B.A., 2012. Genomic analysis of reactive astrogliosis. J. Neurosci. 32, 6391–6410. https://doi.org/10.1523/JNEUROSCI.6221-11.2012.

Zhang, L., Uygun, T., Hahn, H.J., Liu, Y., Rivero-Ríos, P., Li, D., Navratna, V., Bristow, E., Luo, G., Kovarzin, A., Bo, Y., Gadde, S., Côté, M., Ko, D.C., Mosalaganti, S., Reinisch, K.M., Weisman, L.S., 2025. VAC14 oligomerization is essential for the function of the FAB1/PIKfyve–VAC14–FIG 4 complex. MBoC 36, ar78. https://doi.org/10.1091/mbc.E24-11-0490.

Zhang, Y., Zolov, S.N., Chow, C.Y., Slutsky, S.G., Richardson, S.C., Piper, R.C., Yang, B., Nau, J.J., Westrick, R.J., Morrison, S.J., Meisler, M.H., Weisman, L.S., 2007. Loss of Vac14, a regulator of the signaling lipid phosphatidylinositol 3,5-bisphosphate, results in neurodegeneration in mice. Proc. Natl. Acad. Sci. U. S. A. 104, 17518–17523. https://doi.org/10.1073/pnas.0702275104.

Zolov, S.N., Bridges, D., Zhang, Y., Lee, W.-W., Riehle, E., Verma, R., Lenk, G.M., Converso-Baran, K., Weide, T., Albin, R.L., Saltiel, A.R., Meisler, M.H., Russell, M.W., Weisman, L.S., 2012. In vivo, Pikfyve generates PI(3,5)P_2, which serves as both a signaling lipid and the major precursor for PI5P. Proc. Natl. Acad. Sci. U. S. A. 109, 17472–17477. https://doi.org/10.1073/pnas.1203106109.